DR. DANIELE CASALBORE (Orcid ID : 0000-0002-0151-6901)

Article type : Themed Issue Paper

Bedforms on the submarine flanks of insular volcanoes: New insights gained from high resolution seafloor surveys

D. Casalbore[1], M.A. Clare[2], E.L. Pope[3], R. Quartau[4,5], A. Bosman[1], F.L. Chiocci[6], C. Romagnoli[7], R. Santos[4,5]

[1] Istituto di Geologia Ambientale e Geoingegneria, Consiglio Nazionale delle Ricerche (IGAG-CNR), Italy

[2] National Oceanography Centre, University of Southampton, Waterfront Campus, Southampton SO14 3ZH, UK

[3]Department of Geography, Durham University, Lower Mountjoy, South Road, Durham, DH1 3LE, UK.

[4] Instituto Hidrográfico, Lisboa, Portugal

[5] Instituto Dom Luiz, Lisboa, Portugal

[6] Dipartimento Scienze della Terra, Sapienza University of Rome, Rome, Italy

[7] Dipartimento Scienze Biologiche, Geologiche e Ambientali, University of Bologna P.za Porta S. Donato 1, 40126, Bologna, Italy

Corresponding author: Daniele Casalbore, daniele.casalbore@uniroma1.it

Associate Editor – Alexandre Normandeau

This article has been accepted for publication and undergone full peer review but has not been through the copyediting, typesetting, pagination and proofreading process, which may lead to differences between this version and the Version of Record. Please cite this article as doi: 10.1111/SED.12725

Short Title – Bedforms in modern marine volcaniclastic settings

ABSTRACT

A comparative analysis of bedform fields along the submarine flanks of insular volcanoes, characterized by different morpho-structural settings, volcanic and meteo-marine regimes (Vanuatu, Kermadec, Bismark, Madeira and Aeolian archipelagos), is presented here to provide insights on the size distribution, morpho-dynamic and genesis of such bedforms. Two main types of bedforms are recognized according to their size, location and preconditioning/triggering processes. Small-scale bedforms have wavelengths of tens to hundreds of metres and wave heights of metres. Because of their small-size, they are typically not recognizable at water depths greater than 400 m from vessel-mounted bathymetric surveys. However, few examples of small-scale bedforms are reported from upper volcanic flanks, where steep gradients commonly hinder their formation. Their recognition is mostly limited to the thalweg of shallow and flat-bottomed channels that carve the insular shelf on slope gradients <15°. Small-scale bedforms are mostly related to erosional–depositional processes due to sedimentary gravity flows that are often the result of a cascading effect between volcanic and non-volcanic processes (for example, flood discharges and retrogressive landslides). Large-scale bedforms occur at all water depths, having wavelengths of hundreds/thousands of metres and wave heights up to few hundreds of metres. The origin of large bedforms is more difficult to ascertain, especially if only bathymetric data are available. Some diagnostic criteria are presented to distinguish between bedforms associated with landslide deposits and those associated with density currents. In this latter case, relevant sediment sources and slope gradients (<8°) are key factors for bedform development. Erosional–depositional bedforms are typically related to eruption-fed density flows formed during large caldera collapses or to large turbidity flows. Bedforms generated by turbidity flows are often observed in the lower volcanic flanks, where an abrupt decrease of gradients is present, often matching a change from confined to unconfined settings. In summary, this study provides insights to interpret bedforms in modern and ancient marine volcaniclastic settings elsewhere.

Keywords

Multibeam bathymetry, sediment waves, turbidity currents, upper-flow regime, volcanic islands.

INTRODUCTION

Insular volcanoes are highly dynamic environments, where the interplay between volcanic, volcanic–tectonic and erosional–depositional processes contribute to rapidly change their morphology (Casalbore, 2018, and references therein; Ramalho *et al.*, 2013). Volcanic activity also has a strong influence offshore, because of its potential to rapidly delivery large amounts of volcaniclastic material, thus altering 'normal' rates of sedimentation. The large amount of volcaniclastic material available coupled with the steepness of volcanic island flanks promotes widespread mass-wasting processes ranging across different spatial and temporal scales (e.g. McGuire *et al.*, 2006). This greatly contributes to enlargement of submarine edifices by offshore growth of insular volcaniclastic aprons (Menard, 1956; Carey, 2000).

Volcanic islands typically represent the tip of large volcanic edifices rising thousands of metres above the seafloor. Marine studies are therefore essential to fully understand the morpho-structural evolution of their edifices and the erosive–depositional processes acting across the flanks. In the last few decades understanding of the submarine morphology of insular volcanoes has exponentially increased with the advent of modern seafloor mapping (e.g. Mitchell *et al.*, 2002; Coombs *et al.*, 2007; Boudon *et al.*, 2007; Leat *et al.*, 2010; Romagnoli *et al.*, 2013a). However, with a few exceptions, their shallow water portions remain poorly surveyed (Mitchell *et al.*, 2008; Babonneau *et al.*, 2013; Bosman *et al.*, 2014; Casalbore *et al.*, 2015, 2018; Quartau *et al.*, 2015; Ricchi *et al.*, 2018; Clare *et al.*, 2018). Nonetheless, these studies have confirmed that mass-wasting processes play a key role in the morphological evolution of submarine volcanic flanks and can pose a major hazard to offshore infrastructure (for example, subsea telecommunication cables, Carter *et al.*, 2014; Pope *et al.*, 2017) and coastal communities through coastal retrogressive failure and/or tsunami generation (Chiocci *et al.*, 2008; Tappin *et al.*, 2008; Omira *et al.*, 2016; Chiocci and Casalbore, 2017; Williams *et al.*, 2019). Despite most of the attention being focused on the characterization of large-scale slope failures, a suite of smaller geomorphic features associated with erosional–depositional processes have been identified along the submarine volcanic flanks, such as gullies, furrows, channels and canyons, fan-shaped deposits, scours and bedforms (Casalbore, 2018, and references therein).

The recognition of widespread fields of bedforms in modern marine volcaniclastic systems at multiple locations worldwide has recently attracted the attention of marine geoscientists, as demonstrated by the growing number of studies in literature (e.g. Wynn *et al.*, 2000; Wright *et al.*, 2006; Hoffman *et al.*, 2008; Silver *et al.*, 2009; Gardner, 2010; Leat *et al.*, 2010; Sisavath *et al.*, 2011; Casalbore *et al.*, 2014; Mazuel *et al.*, 2016; Pope *et al.*, 2018; Clare *et al.*, 2018; Quartau *et*

al., 2018; Santos *et al.*, 2019). These bedforms can extend over tens of kilometres; individual bedforms having wave heights and wavelengths of hundreds and thousands of metres, respectively. These features are (at least) an order of magnitude greater than the largest volcaniclastic bedforms recognized on subaerial volcanic flanks (Pope *et al.*, 2018, and references therein). They can result from: (i) seafloor deformation due to gravity driven instabilities; (ii) the interaction between sediment-laden gravity flows (associated with flood discharge or eruption-fed pyroclastic flows) and the seafloor; or (iii) a combination of both processes. Pope *et al.* (2018) recently presented some morphological criteria to discriminate between bedforms generated by gravity instabilities and those generated by sediment-laden gravity flows. However, this and other studies identified the requirement for high-resolution seismic datasets to prevent erroneous interpretations (Pope *et al.*, 2018; Quartau *et al.*, 2018). Thus, despite the growing interest in these features, the interpretation of their emplacement mechanism often remains ambiguous.

In addition to the larger scale bedforms, small-scale and crescentic bedforms with wavelengths of tens/hundreds of metres and maximum wave heights of a couple of metres have also been identified on the upper and shallower flanks of insular volcanoes (Babonneau *et al.*, 2013; Romagnoli *et al.*, 2012; Chiocci *et al.*, 2013; Casalbore *et al.*, 2017a; Clare *et al.*, 2018). Although not as widely documented, understanding how these bedforms form can provide useful insight into the transfer of material from subaerial to the deeper marine flanks of insular volcanoes, which has broad relevance for hazards assessment.

The aim of this paper is to provide a comprehensive review of bedforms found in modern marine volcanic settings. This is based on the analysis and comparison of several (published and unpublished) case-studies from volcanic edifices in a range of different geodynamic settings and characterized by different volcano-tectonic evolution (Fig. 1). This study used mainly multibeam bathymetry data integrated (where available) with seismic profiles and seafloor samples. For each identified bedform field, a series of morphological/morphometric parameters were extracted, including water depth range, minimum and maximum slope gradients, wavelengths, wave heights, lateral extent, slope gradients, cross-section and plan view shape of their crestlines. Local boundary conditions are also summarised including morphological settings, volcanic, meteorological and oceanographic regime, and sediment sources, characterizing the locations where these features form in order to understand the main processes responsible for their development. Through synthesis of these data, the aim of this study is: (i) to perform a comparative analysis of bedforms in modern volcaniclastic settings aimed at better understanding

their formation; in particular criteria are provided to distinguish between bedforms associated with cyclic erosional–depositional processes or seafloor displacement due to slope failures; (ii) to analyse the morphology and size distribution of bedforms associated with sediment-laden gravity flows and verify whether the spatial gap identified by Symons *et al.* (2016) between small-scale and large-scale sediment waves in marine settings also applies to volcaniclastic bedforms; (iii) to provide some insights on the morpho-dynamic evolution of the erosional–depositional bedforms and constrain the associated controlling factors; and (iv) to identify the main predisposing and triggering factors for the development of sediment-laden gravity flows in marine volcaniclastic settings and to evaluate their role (in terms of type and magnitude) in controlling the morphological variability and size distribution of volcaniclastic bedforms. The *Conclusion* attempts to highlight outstanding uncertainties in the understanding of bedforms in marine volcaniclastic settings and propose recommendations to fill these knowledge gaps.

CASE-STUDIES

This section introduces the different case studies that are discussed in this paper (Fig. 1), providing information on the geological setting of each study area and prior observations of seafloor morphology (primarily focused on bedforms). Additional information about these bedforms can be found in the supplementary material and on Tables 1 and 2.

Macauley Volcano

Geological setting

Macauley Island is located in the intra-oceanic Kermadec Arc (Fig. 1) and is the uppermost subaerial edifice of an active submarine stratovolcano (Wright *et al.*, 2006; Shane & Wright, 2011; Barker *et al.*, 2012). Onshore Macauley Island, deposits are dominated by basaltic lavas and phreatomagmatic deposits (Lloyd *et al.*, 1996). These are overlain by the Sandy Bay Tephra Formation and younger basaltic lavas (Lloyd *et al.*, 1996). The Sandy Bay Tephra is the only confidently known silicic activity related to this volcano and consists of a massive lithic basal unit overlain by multiple wet pyroclastic density current and surge deposits (Smith *et al.*, 2003; Barker *et al.*, 2012). The majority of the Macauley volcanic complex is submerged, with the submarine landscape dominated by the Macauley Caldera to the north-west of the island (Fig. 2).

Bedform fields

The flanks of the Macauley volcanic complex are dominated by repetitive bedforms which extend out for >20 km from the rim of Macauley Caldera in the west and >55 km to the east of the

volcanic complex (Fig. 2A). These bedforms occur at water depths ranging from 50 m to >3300 m (Table 1) and cover an area >1750 km^2. Due to a lack of data coverage it was not possible to map their farthest extent. The range of bedform wavelengths and wave heights is 125 to 2450 m and 5 to 200 m, respectively.

Repetitive bedform fields (MC1 and MC2, Fig. 2) extend outward on the south-west and northern flanks of Macauley Volcano for >25 km and cover an area of >320 km^2 and >220 km^2, respectively. On the south-west flank, bedform wavelengths decrease seaward from 1500 m to 250 m, whilst their wave heights decrease from 140 m to 5 m. On average the northern flank is steeper (2.7° versus 1.85°) than the south-west flank. Here, bedform wavelengths and wave heights decrease seaward from 1650 m to 220 m and 160 m to 5 m, respectively. The bedforms of both MC1 and MC2 fields have poorly defined lateral margins and are convex in planform (Fig. 2A). In bathymetric profile the lee sides of these bedforms are often steeper and shorter than their stoss sides making the bedforms asymmetrical (Fig. 2D). Although only available perpendicular to the perceived direction of flow for MC1, high-resolution seismic data also indicates that the bedforms are made up of asymmetrical sediment packages (Fig. 2B and C). The seismic data from MC1 shows multiple high amplitude reflectors making up chaotic facies separated from a series of thin, ordered lower amplitude reflectors by a stratigraphic unconformity (Fig. 2C). Although not always detectable, a further internal unconformity exists within the lower amplitude reflectors (Fig. 2B and C). There are >20 planar reflectors beneath this surface and >30 above (Fig. 2C). The lower set of bedform reflectors are truncated at high angles on their lee sides and this forms asymmetrical structures (Fig. 2C). The upper set reflectors are more clearly developed and conform to the underlying unconformity. These reflectors have a dome-like apex and their lee sides are thin but not truncated, instead becoming unresolvable. These characteristics mean that the top set of reflectors are more symmetrical in form than the lower set but remain asymmetrical.

The repetitive bedforms fields, MC3 to MC6 (Fig. 2A), extend outward to the north, east and south of the Macauley volcanic complex for >55 km. These bedforms occur at water depths of 350 to 3300 m and cover a combined area of >545 km^2 (Table 1), extending seaward beyond the available data coverage for this study. The wavelengths of these bedforms range from 125 to 2450 m and their wave heights range from <10 to 200 m (Table 1). However, neither their wavelengths nor their wave heights systematically decrease with distance from the shelf edge. The average slope gradients of MC3 to MC6 are 4.89°, 3.66°, 3.34° and 3.57°, respectively. These are significantly greater than the average slope gradients of bedform fields MC1 and MC2 (Fig. 2D).

Unlike bedforms in MC1 and MC2, the bedforms in MC3 to MC6 have sinuous to linear or concave crestlines (Fig. 2A) and are more symmetrical with flat tops (Fig. 2E). The lateral margins of these bedform fields are also commonly well-defined on the upper flanks of the volcanic complex and often originate from distinct arcuate headwalls (Fig. 2A).

Zavodovski Volcano

Geological setting

Zavodovski Volcano is part of the South Sandwich Arc which is built on the small oceanic Sandwich plate in the South Atlantic (Fig. 1; Larter *et al.*, 2003; Leat *et al.*, 2010). Zavodovski Volcano is *ca* 11.6 km^2 wide and is dominated by a single volcanic cone, Mount Curry (Leat *et al.*, 2010). Zavodovski Island is dominated by basalt and basaltic andesites (Pearce *et al.*, 1995; Leat *et al.*, 2003).

Bedform fields

The eastern flanks of Zavodovski Volcano are characterized by a series of chutes and repetitive bedforms which extend >50 km from the shelf edge (Fig. 3A). The bedform fields, Zd1 to Zd3, occur at water depth ranges of between 160 m and >2800 m and cover an area of >850 km^2 extending eastward beyond the coverage of available bathymetry (Table 1).

Bedform fields Zd1 and Zd3 have the greatest spatial extents, 368 km^2 and >313 km^2, respectively. They also have the greatest bedform wavelengths and wave heights, but both decrease in a seaward direction. Bedform wavelengths in field Zd1, which has the steepest average slope gradient of the bedform fields (2.94°) decrease from 2800 m to 380 m and wave heights decrease from 144 m to 5 m (Table 1). Bedform wavelengths and wave heights in Zd3 (average slope gradient 2.78°) decrease from 2960 m to 285 m and 175 m to 24 m, respectively. Both Zd1 and Zd3 have poorly defined lateral margins. Their planform morphologies are also characterized by changes from concave to convex morphologies with increasing distance offshore (Fig. 3A). In profile, the bedforms of Zd1 and Zd3 are commonly characterized by shorter steep lee sides giving these bedforms a downslope asymmetrical profile (Fig. 3B and D).

Bedform field Zd2 is located between Zd1 and Zd3. It has the smallest spatial extent of the three bedform fields (186 km^2) and is thought to be distinct. Of the bedform fields it has the lowest average slope gradient (1.78°) and smallest wavelength bedforms (900 to 1900 m). The wave

heights of the bedforms are 8 to 164 m. On the upper slope the bedforms are confined within a gully. On the lower slope they are interpreted to be constrained by the bedforms of Zd1 and Zd2 which have conspicuously different wavelengths. Nonetheless, a number of bedforms exhibit a continuity in crestline from Zd1 and Zd3 into Zd3. The Zd2 planform morphologies are predominantly characterized by concave morphologies. In profile, upper to mid-slope bedforms often have short stoss sides and long lee sides (Fig. 3C). Only in the lower slope are the shorter lee sides observed in Zd1 and Zd3 (Fig. 3C).

Dakataua Caldera and Kimbe Bay

Geological setting

Dakataua Caldera and Kimbe Bay are located on New Britain and are part of the Bismark Volcanic Arc (Fig. 1; Silver *et al.*, 1991). Dakataua Caldera lies at the northern tip of the Willaumez Peninsula and is thought to have collapsed 1270 to 1350 years ago (Neall *et al.*, 2008). The eruptive histories of Dakataua Caldera and Mt Makalia, which is currently located within the caldera, are dominated by andesitic lavas and ash deposits. Some porphyritic basaltic andesites and dacitic flows have also been observed (Lowder & Carmichael, 1970). In contrast to other examples in this study, Kimbe Bay is flanked by multiple volcanoes, including Witori and Mt Garbuna, and multiple small rivers which drain them (Hoffmann *et al.*, 2008; Neall *et al.*, 2008). Volcanic products from Witori and the surrounding volcanoes are dominated by a combination of basaltic andesite and andesite, although basalts and dacites are also present (Blake & Bleeker, 1970).

Bedform fields

Two repetitive bedform fields extend from the northern flanks of Dakataua Caldera for *ca* 30 km (Fig. 4A). To the north-east there is also an area of large blocks *ca* 30 km^2 wide, which are believed to have been deposited by a previous sector collapse (Silver *et al.*, 2009). The two bedform fields, DC1 and DC2, occur at water depth ranges of between 1450 m and 2100 m and cover areas of 550 km^2 and 520 km^2, respectively (Table 1). DC1 has the lower average slope gradient (0.9° versus 1.63°). Here, bedforms decrease in wavelength and wave height with distance from the Dakataua Caldera from 3500 m to 384 m and 92 m to 5 m, respectively. The bedform wavelengths and wave heights in DC2 similarly decrease from 2860 m to 820 m and 115 m to 10 m, respectively (Table 1). Both DC1 and DC2 areas have poorly defined lateral margins.

However, the bedforms fields have contrasting morphologies. Bedforms in DC1 are characterized by sinuous to linear planform morphologies (Fig. 4A). The bedforms also show no coherent pattern of asymmetry in profile until water depths >1900 m (Fig. 4B). In contrast, bedforms in DC2 are characterized by convex planform morphologies with observed bifurcation (Fig. 4A). They also commonly exhibit asymmetry in profile with shorter steeper lee sides (Fig. 4C).

The seafloor at the centre of Kimbe Bay is dominated by a field of repetitive bedforms which extends >40 km in a NNW–SSE direction (Figs 1 and 5A). The Kimbe Bay bedforms occur between water depths of 1500 m and 2200 on an average slope gradient of 0.8°. The bedforms have wavelengths of 494 m to 3400 m and wave heights of 7 m to 84 m. The lateral margins of the Kimbe Bay bedform field is poorly defined on its northern and western edges. To the east, it is constrained by a crevice and the Kimbe Bay Escarpment (Fig. 5A). In planform the bedforms are predominantly characterized by convex morphologies and bifurcation is common (Fig. 5A). In profile, there is large variability in the symmetry of the bedforms, ranging from strongly downslope to strongly upslope asymmetry (Fig 5B).

Aeolian Archipelago

Geological setting

The Aeolian archipelago is the subaerial part of a 200 km wide volcanic arc located in the Southern Tyrrhenian Sea (Fig. 1 and Fig. 1 ESM, i.e. Electronic Supplementary Material). Aeolian volcanism is considered to be subduction related and is associated with rifting processes developing within the arc collision zone (Ventura, 2013, and references therein). Volcanic activity ranges from effusive to explosive (from Strombolian to Plinian). Explosive eruptive activity has occurred on Salina and Panarea during the Late-Quaternary (Lucchi *et al.*, 2013). Whilst Stromboli is characterized by persistent Strombolian activity (Rosi *et al.*, 2000), Vulcano and Lipari are characterized by historical eruptions (AD 1888 to 1890 vulcanian-type eruption and AD 1230 obsidian flows, respectively).

Bedforms

Large-scale bedforms have previously been presented in Casalbore *et al.* (2014). The morphological/sedimentological characteristics of the bedforms are summarised in Table 1 (Str1, Str2, Str3, Pan1, Vul1 and Lip1) and briefly presented in the ESM. Small-scale bedforms are instead described in detail below.

Stromboli

Small-scale bedforms (Str 4 in Fig. 1 ESM) are found at water depths of 30 to 170 m within a 600 m wide flat-bottomed channel (Piscità Channel, Fig. 6A). Bedforms have wavelengths of 20 to 86 m and wave heights of 1 to 5 m. Their crestlines are arcuate to crescentic and are generally downslope asymmetrical in cross section with steep (up to 28°) lee sides (profile A–A' in Fig. 6). Bedform size tends to increase downslope in spite of the superposition of smaller bedforms on large ones (Fig. 6). Bedforms generally develop as coaxial trains within narrow and shallow channelized features, whose headwall is defined by semi-circular, fresh-looking landslide scars affecting the littoral wedge up to water depths of 5 m, less than 100 m from the coastline (Fig. 6A).

Repeated bathymetric measurements from 2002 to 2015 (Fig. 6B and C) indicate that significant morphological change occurred in the channel during or just after the main eruptive crisis affecting Stromboli in 2002, 2007 and 2014. The difference map in Fig. 6B shows major bathymetric changes in the easternmost part of the channel, with an overall deepening of the seafloor after the December 2002 eruption. Specifically, the comparison of bathymetric profiles performed on pre-2002 and post-2002 eruption digital elevation models (DEMs) evidences an overall upslope migration of the bedforms (profile B–B' in Fig. 6; see also Casalbore *et al.*, 2017a). The difference map in Fig. 6C also shows major changes in the easternmost part of the channel after the 2014 eruption, but in that case a seafloor accretion of some metres is mostly observed between -80 m and -120 m, whereas patches of seafloor erosion and accretion are recognizable at shallower water depths. The comparison of bathymetric profiles performed on pre-2014 and post-2014 eruption DEMs (profile C–C' in Fig. 6) evidences the formation of a new coaxial train of bedforms after the eruption.

Salina

Small-scale bedforms have been identified along the north and east flanks of Salina (Sal1 and Sal2, respectively, in Fig. 1 in ESM and in Table1).

The northern bedform field is located within a 1 km wide, flat-bottomed channel (North Salina Channel, Fig. 7), whose headwall incises the outer edge of the insular shelf. Here, from 285 to 677 m, arcuate to crescent-shaped bedforms are observed with wavelengths of 44 to 215 m and wave heights of *ca* 1 to 6 m. In cross-section, the bedforms are mostly characterized by downslope asymmetry, with steep lee sides (up to 20°, profiles in Fig. 7). Bedform size generally increases

downslope. In contrast to bedforms in the Piscità Channel, bedforms in the North Salina Channel show little evidence of morphological change over the 11 years of repeated surveys (Casalbore *et al.*, 2017a). Minicores performed on grab samples from the North Salina Channel recovered coarse-grained sand in the lower part of the deposit (locally with gravel), transitioning to find-sand or sandy silt to silty mud in its upper part (Casalbore *et al.*, 2013).

The eastern bedform fields offshore Salina are the result of the coalescence of several coaxial trains of bedforms associated with different channels (Fig. 8). Here, the channel headwalls are located a few tens of metres from the coastline at water depths of 5 to 10 m. These arcuate to crescentic-shaped bedforms are found at water depth of 45 to 430 m with wavelengths of 12 to 153 m and wave heights of 0.2 to 5.4 m. They are downslope asymmetrical with short and steep (up to 30°) lee sides (profiles in Fig. 8). Trains of bedforms begin within narrow and shallow channels as well as fan-shaped features, merging downslope in a wide, flat-bottomed channel (Section c–c' in Fig. 8). A progressive increase of wavelength and lateral extent with water depth is observed. This is associated with a decrease in slope gradient and channel enlargement, or the development of fan-shaped features. Compared to previous examples, wave height shows a more scattered distribution, with a general increase in correspondence with the narrow and confined channelized features. Superimposition of different trains of bedforms with different sizes is also observed. Grab samples from this bedform field mainly recovered fine/medium sand on the upper part of the submarine flank, passing downslope to a silty sand.

Vulcano

Small-scale bedforms were identified on the northwest and northeast submarine flanks of Vulcano (Vul2 and Vul3, respectively, in Fig. 1 ESM and in Table 1). The north-west bedform field (Vul2 in Fig. 9) is formed from a coaxial train along the thalweg of flat-bottomed channels between 200 m and 450 m (where data resolution strongly decreases) on slope gradients of 3° to 9°. Bedforms have wavelengths and wave heights of 30 to 106 m and 1.2 to 3.8 m, respectively. They are mostly downslope asymmetrical with steep lee sides (profiles A–A' and B–B' in Fig. 9). Bedform size generally increases downslope, but strongly depends on channel shape.

Offshore north-east Vulcano, bedforms are present in a few narrow gullies draining the submarine part of La Fossa Caldera from 70 to 200 m on slopes of 7° to 9° (Fig. 9). These crescent-shaped bedforms have wavelengths of 21 to 62 m and wave heights of 0.7 to 2.8 m. They are mostly downslope asymmetrical in cross-section with steeper lee sides. Downslope, larger bedforms are

recognizable on the Baia di Levante fan between 500 m and 800 m on slope gradient of 5° to 7° (Vul3 in Fig. 9). These bedforms have wavelengths of 36 to 92 m and wave heights of 1 to 4 m. They are downslope asymmetrical in cross-section (profile C–C') with sinuous crestlines in plan-view.

Tanna Island

Geological setting

Tanna Island is located in the Vanuatu volcanic arc in the south-west Pacific (Fig. 1). Volcanism on Tanna Island is currently focussed on Mount Yasur, which is a scoria cone formed from repeated strombolian-style and vulcanian-style eruptions that occur every few minutes (Nairn *et al.*, 1988; Merle *et al.*, 2013). Yasur has been fed by a steady state magma reservoir for at least the last 600 years (Nairn *et al.*, 1988; Merle *et al.*, 2013; Firth *et al.*, 2014); however, there is evidence for at least two major ignimbrite-forming eruptions that occurred approximately 43 ka and 3 to 8 ka (Firth *et al.*, 2015) and formed the complex Siwi ring fracture which extends offshore; although its expression is locally obscured by more recent seafloor sediment transport (Clare *et al.*, 2018). Tanna Island is extremely tectonically active. Shallow magma intrusion drives significant post-caldera uplift, with uplift rates of 156 mm/year calculated over the last 1000 years (Chen *et al.*, 1995). Two earthquake events in AD 1878 caused up to 12 m of vertical co-seismic uplift of the coastline (Clare *et al.*, 2018). While these volcanically-driven ground movements are very likely to influence offshore sediment transport, the main triggers attributed to recent offshore turbidity currents are related to non-volcanic events, including elevated sediment discharges from rivers and the coastline during tropical cyclones, and a volcanic lake outburst flood that occurred in AD 2000 (Clare *et al.*, 2018).

Bedform fields

The area surveyed offshore Tanna shows an abundance of asymmetrical bedforms, which are typically crescentic in planform, with low angle upstream stoss sides and steeper angle downstream lee sides (Fig. 10). Four bedform fields are defined. First, is a broadly channelized field of bedforms (Vn1) that initiates close to the offshore outflow of the Siwi River (Fig. 10A, B and C). Here, bedform trains are of low wave height (*ca* 0.3 to 2.0 m) and wavelength (10 to 15 m); however, where bedform trains and channels coalesce into broader fairways away from the source, they tend to increase in size (*ca* 2 to 6 m wave height, up to 180 m wavelength). Stoss-

sides are generally 1 to 3˚, with lee-sides of up to 25˚. The bedform field generally broadens from 10 m wide near the Siwi River outflow (20 m water depth), to 400 m on an unconfined slope at 250 m water depth. However, bedform size does not solely relate to distance from source. Zones of larger bedforms with a higher wavelength to wave height ratio than the rest of the surveyed area are found immediately seaward of the submerged ring fracture (i.e. past caldera collapse). Grain size analysis from crescentic bedforms in the submarine bedform field offshore from Siwi River reveals a very similar distribution to that of samples from the river (mean grain size of *ca* 400 μm), with clear bimodality at the most proximal location, becoming progressively finer (mean grain size of *ca* 100 μm) offshore (Clare *et al.*, 2018). Transmitted light and scanning electron microscopy show that sediment is dominantly comprised of basaltic lithics with a small component of volcanic glass. Small amounts of carbonate and coralline debris are incorporated further offshore. No sampling was possible in the other bedform fields, and hence is not reported. The second bedform field (Vn2), is headed by steep linear gullies that feed into a sinuous channel, which becomes deflected by a remnant block (from the last phase of caldera collapse, Fig. 10D). Here, bedforms reach 0.2 to 8.5 m wave height, with wavelengths of *ca* 5 to 80 m. Stoss-sides are generally 1 to 3˚, with lee-sides of up to 30˚. The third bedform field (Vn3, Fig. 10A), is represented by a linear channel (also fed by gullies) with bedforms of similar scale to Vn2 (Table 1). Finally, the fourth bedform field (Vn4, Fig. 10A), occurs down-stream of a carbonate platform fringed by reefs, and includes a broad (up to 200 m wide) linear channel. Bedforms within Vn4 are up to 6 m in height with wavelengths of up to 60 m.

Madeira Archipelago

Geological setting

The Madeira Archipelago is located in the north-east Atlantic, ca 1000 km south-west of the Iberian Peninsula (Fig. 1). It comprises the islands of Madeira, Porto Santo, Desertas and Selvagens.

Madeira is the youngest island, with volcanism spanning 7 Ma to the Holocene (Geldmacher *et al.*, 2000; Ramalho *et al.*, 2015). It is an elongated shield volcano, and the island is highly dissected by subaerial erosion, but still with ca 25% above 1000 m. Annually, Madeira receives 600 mm of precipitation at sea level and 3000 mm in the highest elevation. Unevenly distributed throughout the year, intense rainfall events make the island very prone to flash floods and related subaerial landslides (Baioni, 2011).

The Desertas Islands are the subaerial expression of a 50 km long NNW–SSE trending arm. These islands were heavily destroyed by wave erosion and landsliding. The volcanism of Desertas shows many similarities with Madeira's, although its volcanic activity stopped 1.9 Ma (Schwarz *et al.*, 2005).

Porto Santo is much older than Madeira and Desertas, with volcanic activity confined to 14 to 10 Ma (Schmidt & Schmincke, 2002). Surrounded by a wide shelf (up to 14 km), it has experienced significant erosion. It receives <400 mm of precipitation on average and has an ephemeral subaerial drainage system that only flows after heavy rainfall.

The Selvagens consist of two groups of islands and islets (Santos *et al.*, 2019). The north-east group consists of two small islets and Selvagem Grande that is basically a cliff-bounded plateau, 80 to 100 m in elevation. The south-west group is composed of Selvagem Pequena, having an average height of 10 m, and numerous small islets. The subaerial history of Selvagem Grande comprises three volcanic stages and two erosional stages, spanning a period of volcanic activity of 26 to 3 Ma (Geldmacher *et al.*, 2001). The subaerial part of the Selvagem Pequena is dominantly composed of rocks from the older volcanic stages, dated *ca* 29 Ma (Geldmacher *et al.*, 2001).

Bedform fields

The examples described below represent the different types of bedform fields found on Madeira Archipelago. The remaining bedform fields show similar settings and interpretations and are therefore presented in the ESM and summarised in Tables 1 and 2.

East of Desertas

A large bedform field (MA1 in Figs 11 and 2 ESM) with *ca* 1900 km^2, occurs east of Desertas Islands at 2900 to 4300 m water depth (wd) (Quartau *et al.*, 2018). The bedforms are sinuous in plan-view and can be divided into two areas by their morphological setting. The southern field (limited by the dashed black lines in Fig. 11 and characterized by profiles DS1 and DS2) occurs offshore an 11 km long shelf edge scar (Fig. 11). It is composed of bedforms with wave heights of 5 to 31 m and wavelengths of 746 to 3014 m. In cross-section, bedforms change from downslope asymmetrical to upslope asymmetrical. The northern field occurs at the end of channels which drain the eastern submarine slopes of Desertas (DS3 to DS4, Fig. 11). Here, bedforms are larger with wave heights and wavelengths of 8 to 47 m and 1016 to 4352 m, respectively. Cross-sectional profiles are similar to the southern field bedforms. In general, bedforms of MA1 tend to increase

in wavelength and decrease in wave height with water depth. In both cases the bedforms start at the transition from high-slope gradients to gradients smaller than 5º.

South of Porto Santo

A small (*ca* 150 km^2) bedform field (MA2, Fig. 11; Fig. 2 ESM) occurs south of Porto Santo Island at 3250 to 4000 m wd, offshore a 13 km long shelf edge scar (Fig. 11). The bedform trains have wave heights of 19 to 124 m and wavelengths of 1369 to 2322 m. They are sinuous in plan-view and upslope asymmetrical to symmetrical in cross-section (PS1, Fig. 12). The bedforms start at the transition from high-slope gradients to gradients smaller than 5º.

North of Porto Santo

A large (*ca* 1500 km^2) bedform field (MA3, Fig.12 and Fig. 2 ESM), occurs north of Porto Santo Island at 2500 to 3600 m. The bedform field can be divided into to two areas according to their setting. The more eastern field, confined by the black dashed lines (Fig. 12), with a fan shape; and a western one, with an indistinct shape. The fan-shaped field is formed by a series of channels and interfluves that originate from an arcuate headwall scar at the northern shelf edge of Porto Santo and show a divergent geometry. The bedforms inside the channels (PS2 and PS3 in Fig. 12) are crescentic downslope in plan-view and change between upslope asymmetrical and symmetrical in cross-section (a few are downslope asymmetrical). They are 2 to 16 m high with wavelengths of 228 to 983 m. The interfluve bedforms (PS4 in Fig. 12) are crescentic upslope in plan-view and change between upslope asymmetrical, downslope asymmetrical and symmetrical in cross-section. They are significantly larger than those in the channels with wave heights of 4 to 35 m and wavelengths of 706 to 1248 m. West of the fan-shaped field, the bedforms (PS5 in Fig. 12) occur mostly north of a 25 km long submarine ridge that originates on the north-west tip of the Porto Santo shelf edge. These bedforms are less defined and more irregular in plan-view. However, their cross-section shape and size are very similar to those on the interfluves. All of these bedforms start at the transition from high-slope gradients to gradients smaller than 5º.

South of Selvagens

A small bedform field (SEL1 in Fig. 13 and 2 ESM) with *ca* 180 km^2, occurs south of Selvagens at 2300 to 3400 m water depth. The bedform field can be divided in two areas according to their morphological setting (see profiles SV1 and SV2 in Fig. 13). A more eastern and deeper one (profile SV2 in Fig. 13) that starts at *ca* 3000 m water depth and a more western and shallower one (profile SV1 in Fig. 13) that starts at 2300 m water depth. The eastern field occurs at the end of

channels that dissect the submarine slopes of island, originating at the shelf edge of Selvagem Grande as headwall scars. These bedforms are 1 to 17 m in height and 188 to 1071 in wavelength, are sinuous in plan-view, and change between upslope asymmetrical and symmetrical in cross-section. The more western bedforms are similar in plan-view and cross-section view but are significantly larger, 2 to 42 m in height and 345 to 1542 in wavelength. These occur on the base of a volcanic ridge linking Selvagem Grande to Selvagem Pequena, and also at the end of smaller channels that dissect the slopes of the ridge. On both cases the bedforms start at the transition from high-slope gradients to gradients smaller than 5º.

South-west of Selvagens

A bedform field (SEL4 in Fig. 13) occurs at a different setting than the previous ones, and slightly deeper (3300 to 3600 m). The base of the submarine slopes of Selvagens are marked by several scour features, with rectangular or u-shaped in headwall scars in cross-section which are 3 to 30 km wide, 10 to 20 km long and 40 to 100 m deep (Santos *et al.*, 2019). The bedform field, of 50 km^2, occurs at water depths of 3300 to 3600 m immediately offshore of the biggest scour. The bedforms have wave heights of 1 to 10 m and wavelengths of 198 to 784 m, respectively, and are dominantly symmetrical in cross-section. They are not distinguishable in plan-view due to *ca* 128 m cell-size of the bathymetry at these water depths.

DISCUSSION

Genesis of bedforms in modern marine volcaniclastic settings: difficulties and criteria to distinguish between cyclic erosional–depositional processes or seafloor displacement due to slope failures

The previous section has shown bedforms to be widespread in modern marine volcaniclastic settings and display large variability in their size, morphology and location. The recognized bedforms are generally characterized by crescent-shaped or sinuous crestlines that are roughly aligned perpendicular to the regional slope gradient, indicating that gravity-driven processes play a dominant role in their development. Their genesis can be related to two main kinds of processes: cyclic erosional–depositional processes associated with sediment-laden gravity/eruption-fed pyroclastic flows and seafloor displacements due to slope failures. Based on the presented case-studies integrated with examples from literature, we discuss the possible criteria and difficulties for interpreting the main processes behind the formation of small- and large-scale bedforms (for

their morphological characteristics see *Morphology and size of bedforms associated to sediment-laden gravity flows in modern marine volcaniclastic setting: is there a real distinction between small-scale and large-scale bedforms?* section and Fig. 14) in modern volcaniclastic settings.

The small-scale bedforms identified in the upper submarine flanks of the Aeolian Islands (Figs 6 to 9), Vanuatu (Fig. 10) and La Reunion Islands (Babonneau *et al.*, 2013) are very similar in size and morphology to upper-flow regime bedforms found in many other subaqueous, non-volcanic settings where repeated seafloor surveys and direct flow monitoring have demonstrated the occurrence of turbidity currents that undergo a series of hydraulic jumps (Hughes-Clarke, 2016; Normandeau *et al.*, 2016; Hage *et al.*, 2019; Paull *et al.*, 2018; Vendettuoli *et al.*, 2019). Similarly, repeated multibeam surveys performed at Piscità Channel (Stromboli, Fig. 6) evidenced an overall upslope migration of the bedforms through time (profile B–B' in Fig. 6; Casalbore *et al.*, 2017a), a feature typically associated with upper-flow regime bedforms (e.g. Slootman & Cartigny, 2019, and references therein). In the other case-studies, repeated multibeam surveys are not available, but the arcuate shape of bedform crests mainly curving downslope near the sides of a channel, is indicative of higher current velocities in the centre of the channel associated with an overall upslope direction of migration, supporting their interpretation as upper-flow regime bedforms (Cartigny *et al.*, 2011; Symons *et al.*, 2016).

The interpretation of large-scale bedforms is often more complex, especially if only bathymetric data are available. The main diagnostic criterion for discriminating their origin is the analysis of their internal geometry using seismic profiles, similarly to what was proposed for large-scale bedforms in non-volcanic settings (Lee *et al.*, 2002; Li *et al.*, 2019). For instance, the seismic profiles crossing the MC1 field at Maucaley volcano (Fig. 2B and C) show that these bedforms are characterized by internal seismic reflectors with lateral continuity and architecture suggestive of overall upslope migration, allowing them to be interpreted as upper-flow regime bedforms (for a full discussion see *Predisposing/triggering factors for the development of sedimentary gravity flows in marine volcaniclastic settings* section; Pope *et al.*, 2018). However, it should be noted that the acquisition of seismic profiles able to image the inner geometry of bedforms is often hindered along the flanks of volcanic edifices, because they are commonly characterized by steep slopes and coarse-grained sediments or rocky outcrops. In such cases, the only available data for their interpretation is multibeam bathymetry. Below different 'morphological' criteria are recommended to constrain the origin of bedforms, updating the previous guidelines proposed by Pope *et al.* (2018):

1 Morphological setting: bedforms generated by slope failures are generally confined within the scar headwall or by two well-defined lateral margins in their upper reaches, while they are absent from the nearby interfluves. Alternatively, these bedforms can develop over a compressional zone at the toe of the landslide scar, representing the morphological expression of pressure ridges and thrusts (e.g. Bull *et al.*, 2009, and references therein). In the case-studies herein, examples of bedforms generated by slope failures are recognizable on the northern (MC3) and southern (MC6) flanks of Maucaley edifice (Fig. 2; Pope *et al.*, 2018), where the bedforms are confined within landslide scars. Here, bedforms have sinuous to linear or concave crestlines and symmetrical cross-sections with flat tops, suggesting the occurrence of rotated blocks. Conversely, bedforms generated by sedimentary gravity flows are related to the development of large volcaniclastic turbiditic systems. In such settings, these bedforms occur in association with canyons/channels, gullies and troughs, scour features, overbanking deposits, fan-shaped features and depositional lobes. Impressive examples of large-scale bedforms associated with volcaniclastic fans have been reported around La Reunion Island, where they are interpreted as the result of unconfined gravity flows, mainly supplied from riverine input (Mazuel *et al.*, 2016). In the present case-studies, different examples of bedforms generated by unconfined flows can be observed along the lower flanks of Madeira Archipelago (MA1 to MA5, SEL1 to SEL4 in Fig. 11, 12, 13, 2ESM and 3ESM; Quartau *et al.*, 2018; Santos *et al.*, 2019), Stromboli and Panarea islands (Str1 to Str3; Pan1 in Fig. 1ESM; Casalbore *et al.*, 2014):

2 Slope gradients: bedforms generated by slope failures can occur over a large range of slope gradients, especially on higher slope gradients that favour the development of landslides (e.g. Leat *et al.*, 2010; Chiocci *et al.*, 2013), whereas bedforms generated by cyclic erosional–depositional processes occur only below a certain threshold of slope gradients because this parameter strongly controls the rheological behaviour of sedimentary gravity flows, as largely discussed in the following two sections;

3 Along-slope variations in bedform morphometry: bedforms generated by slope failures show little to no downslope change in geometry. Conversely, bedforms generated by sedimentary gravity flows commonly show a decrease or increase of bedform morphometry in relation to changes in flow thickness, velocity and specific discharge as evidenced by previous studies on turbidity current-related sediment waves (e.g. Wynn *et al.*, 2002; Cartigny *et al.*, 2011; Postma & Cartigny, 2014). Such bedforms are very sensitive to abrupt changes in slope gradients as those commonly observed in the lower part of volcanic flanks, where sedimentary gravity flows pass

through a hydraulic jump as they significantly thicken and decelerate (e.g. Postma *et al.*, 2009; Spinewine *et al.*, 2009).

It should be noted that there are often cases where a discrimination between the two processes (slope failure versus sedimentary gravity flows) is very difficult, or a combination of both processes is possible. The rough morphology created by landslide deposits may, in fact, enhance the successive development of erosional–depositional bedforms as sediment density flows cross those areas.

This mechanism has been for instance proposed for the bedform field Vul1 developed along the south-west flank of Vulcano Island (Fig. 1 ESM), where seismic profiles showed the development of undulating reflectors on the irregular top of a semi-transparent and chaotic seismic unit interpreted as a mass transport deposit (Casalbore *et al.*, 2014). This evidence is also supported by the recognition of two normally graded volcaniclastic layers recovered from a gravity core on the bedform field and interpreted as the result of sedimentary gravity flows.

A similar and alternative interpretation is also proposed for the southern part of MA1, MA2, and eastern part of MA3, MA4 and MA5 bedform fields recognized at Madeira Archipelago (Figs 11, 12, 2ESM and 3ESM). These bedforms are associated with distinct large-scale arcuate headwall scars, suggesting a possible origin from seafloor displacement due to landslide deposits. However, they also show a marked change in bedform morphometry along-slope (profiles DS1 to DS3 in Fig. 11, PS2 and PS3 in Fig. 12), just below a significant decrease in slope gradients (*ca* 30° to 20° to <5°) in the lower flank (Quartau *et al.*, 2018; Santos *et al.*, 2019). These findings lead the authors to hypothesize that such bedforms are likely generated by sedimentary gravity flows exploiting the irregular surface of debris avalanche deposits and the slope break present in the lower volcanic flank.

Attributing a definitive formative process for the bedform fields identified at Zavodovski Volcano, Dakataua Caldera or Kimbe Bay is also very difficult. Enclosed depressions that are superimposed on Kimbe Bay bedforms are suggested to relate to deformation (Hoffmann *et al.*, 2011). However, nearby channels and plunge pools suggest sediment density flow activity near the bedform field. Sub-bottom profiler data also shows thicker sediment packages on the upslope limbs of bedforms as well as the upslope migration of sediment packages consistent with sediment density flows (Wynn *et al.*, 2002; Hoffmann *et al.*, 2008; 2011).

Similarly, Zavodovski bedform fields originate from headwalls at the shelf edge and are confined within gullies in their upper reaches, suggesting a landslide/slump origin (Hampton *et al.*, 1996).

However, the planform morphologies of Zd1 and Zd3, similar to those on other volcanic islands attributed to sediment density flows, together with the recognition of overbank sediment deposits in the area and evidence of downslope prograding sediments containing internal reflectors in sub-bottom profiler data (Leat *et al.*, 2010), would indicate an origin from sedimentary gravity flows. The role of sediment gravity flows is also suggested by the lack of bedforms which have developed in the shadow of a volcanic cone (Fig. 3A). In contrast to bedforms in Zd1 and Zd3, bedforms within Zd2 have different waveform geometries and are laterally confined. Both these features are more suggestive of a mass-wasting origin, despite some of the bedforms showing continuity with bedforms in Zd1 or Zd3. As a consequence of the complexity exhibited in all these cases, we thus interpret the Zavodovski bedform fields to be the result of a complex interplay between sediment density flows and mass-wasting processes.

The next sections first discuss the different morphology and size of bedforms associated with sedimentary gravity flows (*Morphology and size of bedforms associated to sediment-laden gravity flows in modern marine volcaniclastic setting: is there a real distinction between small-scale and large-scale bedforms?* section) and then the main processes controlling their formation/morpho-dynamic evolution (*Processes controlling the genesis and morpho-dynamic evolution of the erosive–depositional bedforms* section) and of the associated sedimentary gravity flows as well (*Predisposing/triggering factors for the development of sedimentary gravity flows in marine volcaniclastic settings* section).

Morphology and size of bedforms associated to sediment-laden gravity flows in modern marine volcaniclastic setting: is there a real distinction between small-scale and large-scale bedforms?

The integration of the present data with other examples of submarine volcanic bedforms in the literature allows the authors to make a general distinction between shallow (water depth <400 m), small-scale bedforms (wavelengths of tens/hundreds of metres and wave heights of few/some metres) and deep (water depth >800 m), large-scale bedforms (wavelengths up to kilometres and wave heights up to hundreds of metres) (Fig. 14). The paucity of small-scale bedforms detected in deep volcanic settings is likely due to a technological bias related to the exponential decrease in resolution of vessel-mounted multibeam bathymetry with increasing water depth. Small-scale bedforms are usually unrecognizable at water depths > 400 m (depending on the type and frequency of multibeam system), unless Autonomous Underwater Vehicle (AUV)-mounted or Remotely Operated Vehicle (ROV)-mounted multibeam surveys are performed, as recently observed in the deeper part (down to 1900 m water depth) of active canyon systems off California

(e.g. Paull *et al.*, 2008 and 2010). Here, multibeam system mounted on AUV allowed obtaining bathymetric data with a vertical resolution of 0.15 m and a horizontal footprint of 0.7 m at 50 m survey altitude. On other hand, it is noteworthy that (where data is available) small-scale bedforms are not so common on the upper part of volcanic edifices, especially if compared to non-volcanic settings. This is because volcanic edifices are frequently characterized by steep flanks, with gradients >20° to 30° (Quartau *et al.*, 2010; Romagnoli *et al.*, 2013a), whilst on passive margins, slopes are not steeper than 5º to 10º (O'Grady *et al.*, 2000). On such steep gradients, the sediment-laden flows tend to bypass or erode the seafloor (as evidenced by a network of narrow and steep gullies), hindering the formation of small-scale bedforms (Schlager & Camber, 1986; Micallef & Mountjoy, 2011; Clare *et al.*, 2018). In the present case-studies, small-scale bedforms start to develop only when gradients decrease to values less than 15° (Table 1; Fig. 14). This threshold can vary slightly between the different areas in relation to the morphological setting and characteristics of the source area (sediment type, flow rheology, and so on). This range of gradients on the upper flanks is often associated with the development of shallow and flat-bottomed channels able to incise the shelf, sometimes cutting back up to the coast (Figs 6 to 10). In such cases, a morphological link between these submarine channels and the local drainage network on the island can be envisaged, as discussed in the *Predisposing/triggering factors for the development of sedimentary gravity flows in marine volcaniclastic settings* section (Figs 8 and 10; Babonneau *et al.*, 2013).

Large-scale bedforms occur at all water depths, but they are more commonly observed on the lower part of volcanic flanks. Slope gradients play an important role here also, with the bedforms recognized on slope gradients <8° (especially below 3° to 5°, Table 1; Fig. 14).

The definition of small-scale and large-scale bedforms partially reflects that recently proposed by Symons *et al.* (2016), where a gap in size between these two kinds of bedforms was observed through statistical analysis of several case-studies. However, by plotting the wavelengths and wave heights of all bedforms observed in this study (Fig. 15), the data suggest that there is a continuity of bedform sizes. This continuity can be explained by interpreting the data that fills the gap shown by Symons *et al.* (2016) as end-members of small-scale and large-scale bedforms, respectively. In the opinion of the authors, the subdivision between small-scale and large-scale bedforms is in fact based on process differences:

1 Small-scale bedforms mostly occur in confined settings; however, it is noteworthy that the higher resolution data is typically available in the shallower water portions of the systems that tend

to be more confined, implying a possible methodological bias in their recognition. Their size (especially wavelengths and lateral extent) often tend to increase downslope, partially overlapping the smaller sizes of the large-scale bedforms. This is especially true where there are marked changes in slope gradient and/or the confluence of small gullies in larger and shallower channels (see *Processes controlling the genesis and morpho-dynamic evolution of the erosive-depositional bedforms* section).

2 Large-scale bedforms occur in both confined and unconfined settings. Their size is strongly dependent on the setting, distance from source area and characteristics (frequency and energy) of the sediment-laden flows (see *Processes controlling the genesis and morpho-dynamic evolution of the erosive-depositional bedforms* section). However, where part of the bedform train originates in proximal, confined settings, they commonly display smaller sizes which partially overlap with the larger sizes of small-scale bedforms. It is noteworthy that the recognition of bedforms that fill the spatial gap of Symons *et al.* (2016) is often hard to detect on morpho-bathymetric data acquired with vessel-mounted multibeam systems because of the size (wavelengths of few hundreds of metres and wave heights around 5 to 10 m) and water depth range (i.e. few thousands of metres) where they develop.

Another interesting finding is that the aspect (wave height/wavelength – H/L) ratio of the recognized bedforms shows a very scattered distribution, ranging from values less than 1:10 to values greater than 1:100 (Fig. 15A). However, the data also show that each volcanic setting is characterized by a specific range of this ratio (especially for large-scale bedforms, Fig. 15B) even if overlapping areas are present among the different case-studies. These differences are less accentuated for small-scale bedforms (Fig. 15C), even if it is noteworthy that in the Vanuatu case (Fig. 15C), the H/L ratio enables two main bedform fields to be distinguished within the same area. Here, Vn1 bedforms at water depths <60 m show a similar aspect ratio to the Vn2 to Vn4 bedforms, whereas Vn1 bedforms at water depths >60 m are characterized by a lower H/L occurring just seaward of a caldera collapse margin (Fig. 10). This setting created a locally steeper slope, which may promote erosion and ignition of flows and which are capable of creating larger bedforms (Clare *et al.*, 2018).

Processes controlling the genesis and morpho-dynamic evolution of the erosive–depositional bedforms

In all case-studies, bedforms generated by sediment-laden flows were found at/or close to relevant sediment sources, i.e. large caldera collapses, subaerial/submarine depressions left by sector collapses, shallow submarine channels directly linked to the subaerial drainage networks or able to intercept longshore drift, insular shelf sectors largely indented by landslide scars and/or channelized features, indicating a main role of sediment supply for their formation (Fig. 14). Moreover, the morphological confinement and the regional slope gradient can be considered as a key factor for bedform development. The possibility of a density flow becoming supercritical mostly depends on slope and flow stratification (Postma & Cartigny, 2014). By considering the steepness of the submarine volcanic flanks (with values typically >20° in the upper part) most of the recognized features in this study can be interpreted as upper-flow regime bedforms. Suggestions of the genesis of the recognized bedforms can be provided by comparing their morphology, internal geometry (where available) and downslope changes in bedform morphometry with other case-studies and results from numerical/experimental studies on their formation. In the present case-studies, the step-like cross-section that characterizes most of the bedforms (especially small-scale features), consisting of long and flat to low-angle stoss sides followed by steep and short lee sides is considered a typical feature of cyclic steps (Cartigny *et al.*, 2011; Zhong *et al.*, 2015). The increase of wavelength (with decrease of the aspect ratio) and asymmetry of the recognized bedforms with distance from the source area and decreasing slopes (for example, bathymetric profiles in Figs 8, 9 and 10) is also compatible with a cyclic step origin, similarly to the trend observed for similar features recognized in prodeltaic settings (e.g. Fricke *et al.*, 2015; Normandeau *et al.*, 2016; Hage *et al.*, 2018) and distal submarine channels (Covault *et al.*, 2014 and 2017). Numerical analyses have evidenced that these morphometric parameters depend on several factors, of which initial slope, inflow thickness and flow velocity (the latter two controlling Froude number and discharge) are the most important (e.g. Kostic, 2011; Slootman & Cartigny, 2019). A reduction of slope gradients would force the flow to pass the hydraulic jump at some time, during which the velocity of the flow would be reduced significantly and its thickness markedly increased, favoring the development of bedforms (e.g. Postma *et al.*, 2009; Spinewine *et al.*, 2009). In addition, on steeper slopes acceleration and destabilization of the flow commonly produces smaller wavelength cyclic steps with closely spaced hydraulic jumps (Postma & Cartigny, 2014; Dietrich *et al.*, 2016). By contrast, the decrease of slope gradients should be compensated by an increasing distance required for the acceleration of the flow after each hydraulic jump to reach supercritical condition, so leading to longer wavelengths. This condition

can also cause the formation of a longer stoss side in comparison to the lee side, thus explaining the overall increase in bedform asymmetry downslope. For small-scale bedforms, the increase of the wavelength and lateral extent of the bedforms is often associated with the enlargement of the hosting channel associated with a minor morphological confinement of the flow (Paull *et al.*, 2018), where narrower channelized features converge downslope in a main channel, as observed at Stromboli, Salina, Vulcano and Tanna edifices (Figs 6 to 10). This evidence can be interpreted as due to the progressive increase of specific discharge and flow depth downslope (e.g. Cartigny *et al.*, 2011). These processes can occur as the flow either erodes sediments or becomes more dilute due to sediment deposition and water entrainment (e.g. Normandeau *et al.*, 2016). The main role of the morphological confinement on bedform geometry is also more evident for large-scale bedforms observed in the lower part of the volcanic flank, such as at the Aeolian (Fig. 1ESM) and Madeira archipelagos (Figs 11 to 13 and 3ESM), where a significant increase in wavelength and lateral extent of bedforms is associated with the development of unconfined gravity flows spreading on the seafloor just below abrupt slope breaks. However, it should be stressed that understanding the origin and morpho-dynamics of large-scale bedforms is more complicated than for the small-scale bedforms. Principally, this is a consequence of the lack of direct monitoring of large-scale flows able to form them. The complex internal geometry of these bedforms imaged by the seismic profile crossing the MC1 field in the south-western part of Maucaley edifice strongly supports this thesis (Fig. 2B and C). In this case, the overall bedform symmetry and architecture of these bedforms suggests that stoss-side deposition and lee side erosion occurred during their formation, indicating that the bedforms migrated upstream and are therefore representative of upper-flow regime bedforms (Pope *et al.*, 2018). Of these, the lower set of reflectors is thought to relate to cyclic steps due to their longer wavelength and more asymmetrical shape (Cartigny *et al.*, 2011 and 2014). The upper set is interpreted to be reflective of anti-dunes due to their greater symmetry and apparent conformation to the underlying bedforms. Superposition of more symmetrical bedforms on top of longer cyclic steps has been previously observed both in experiments and modelling and it can be interpreted to reflect a drop in Froude number through time (Cartigny *et al.*, 2014; Kostic, 2014; Zhong *et al.*, 2015). However, it is not known whether this change in bedform type occurred during the same eruptive event reflecting the waxing and waning phases associated with a large explosive eruption or if it is the product of supercritical density flows generated during multiple eruptions of variable magnitude. It is also noteworthy that the wavelengths and wave heights of bedforms at Maucaley tend to decrease with distance from

their envisaged sources. This is in contrast to the previous examples of large-scale bedforms, even if in this case no significant changes in slope gradients or passage from confined to unconfined settings are observed (Fig. 2A and profiles A' and B'). This suggests that sediment concentration, grain size and/or velocity of eruption-fed sedimentary gravity flows decreased with distance, reducing the flow's ability to modify the seafloor (Pope *et al.*, 2018) in agreement with similar observations for other large-scale sediment waves developed in turbiditic systems (e.g. Ercilla *et al.*, 2002).

Predisposing/triggering factors for the development of sedimentary gravity flows in marine volcaniclastic settings

Different predisposing/triggering mechanisms for sediment gravity flows which result in bedform formation in submarine volcaniclastic settings are proposed (Fig. 14), mainly in relation to the size of the bedforms. In many cases they are the result of a compounded or cascading interaction between volcanic and non-volcanic processes (Fig. 14) as recently proposed by Clare *et al.* (2018). In the case of small-scale bedforms, the processes responsible for the formation of the sediment-laden flows are similar to those recognized in non-volcanic settings, but the following attempts to highlight the specificity of the volcanic settings:

1 On most volcanic-arc islands, the development of hyperpycnal flows at river mouths is favoured by small and steep drainage basins that commonly characterize volcanic islands, similar to the so-called dirty-rivers of Mulder & Syvitski (2005). Moreover, recent monitoring has shown that even dilute river plumes may be capable of triggering turbidity currents that can create crescentic bedforms (Hage *et al.*, 2019). In addition, large explosive eruptions can drastically modify the surrounding catchment basins and cause a sudden and large supply of loose easily transported tephras which can greatly increase river sediment loads. This process has been monitored during and immediately after the most important eruptions of Mount Pinatubo (Philippines), especially where lahars acted as temporary dams (Newhall & Punongbayan, 1996). In such cases, once the impounded water is able to overtop the volcanic debris dams, flooding ensued, such as the extremely devastating events in 1991, 1992 and 1994. A quite similar scenario has been recently proposed for the genesis of bedforms at Tanna (Vanuatu, Fig. 10) that can be associated with the impoundment of Lake Isiwi by lava flows and successive outburst floods discharged at the outflow of the Siwi River in 2000 (*Tanna Island* section; Clare *et al.*, 2018);

2 Development of submarine and coastal slope failures can be triggered by seismic/volcanic activity and deformative processes during eruptive events. Such events have been recently observed at Stromboli in 2002 (Chiocci *et al.*, 2008) and Anak Krakatau in 2018 (Williams *et al.*, 2019). At Stromboli, significant morphological variations at the Piscità Channel are recognized only during or after the main eruptive crisis that interrupted the normal 'Strombolian' activity (Fig. 6B and C; Casalbore *et al.*, 2017a).

In such cases, slopes are preconditioned by the progressive infilling and oversteepening of channel heads due to sedimentation driven by subaerial drainage networks or by interception of littoral drift that on active islands can greatly increase during eruptive events. The former process was previously described in point "1" and is well testified by the network of steep creeks draining the large amount of pyroclastic material present on the eastern flank of Salina (Fig. 8). This drainage system may have funnelled volcaniclastic debris into the sea, contributing to the dismantling of the insular shelf, and thus promoting the connection between subaerial and submarine drainage systems, as proposed by Romagnoli *et al.* (2018). The interception of littoral drift has been hypothesized at Stromboli, considering the lack of subaerial water courses facing the Piscità Channel (Fig. 6A). According to Romagnoli *et al.* (2006), increased longshore transport occurs during/after major eruptive crisis when subaerial lava flows entered the sea and large amounts of volcaniclastic debris was produced at Sciara del Fuoco collapse scar (SdF Fig. 1 ESM). This material is transported in a clockwise direction (magenta arrow in Fig. 1 ESM) around the island due to the prevailing westerly winds, feeding the beaches on its north and north-east side, and can be intercepted by the headwall of the Piscità Channel that lies at some metres of water depth, few tens of metres far from the coast (Fig. 6).

In the case of insular volcanoes, small retrogressive failures occur also at the edge of the insular shelf or affect volcaniclastic prograding wedges that commonly overlie the erosive surface of the shelf (Casalbore *et al.*, 2017b; Quartau *et al.,* 2012, 2014, 2015). The formation of these prograding wedges has been related to seaward transport of sand from the surf zone and shoreface during stormy conditions (e.g. Hernandez-Molina *et al.*, 2000; Chiocci & Romagnoli, 2004), so representing a temporary storage area on the shelf for material produced by volcanic activity and coastal erosion. The Vul2 bedform field on the north-west part of Vulcano (Figs 1ESM and 9) and the Sal1 field on the northern flank of Salina (Figs 1ESM and 7) were likely produced by sediment gravity flows associated with retrogressive erosion of the large amounts of volcaniclastic material stored as prograding wedges on the shelf. In the Vulcano case, this material mostly accumulated in

the saddle between Vulcano and Lipari island (Romagnoli *et al.*, 2013b), whereas in the northern part of Salina a large amount of pyroclastic material was recently emitted during the lower Pollara explosive eruptions (15.6 cal ka; Lucchi *et al.*, 2013) forming a coastal cliff exposed to erosion.

Based on the associated preconditioning/triggering processes, two main groups of large-scale bedforms can be recognized:

The first group is associated with volcano-tectonic processes (Fig. 14) and can occur from shallow to deep-water sectors. These bedforms are mostly observed within or downslope of sector collapse depressions (Stromboli, Fig. 1 ESM; Canary Islands, Wynn *et al.*, 2000) as well as around large caldera collapses (Figs 2 and 4; Santorini Island, Bell, 2011). In the former case, sector collapses represent a main pathway for the transport of volcaniclastic material from the islands towards deeper sectors, especially when these areas are fed by persistent volcanic activity and thus able to generate frequent and high-energy sedimentary gravity flows, as for instance observed along the Sciara del Fuoco depression at Stromboli (Kokelaar & Romagnoli, 1995; Romagnoli *et al.*, 2009a, Fig. 1 ESM). In the latter case, bedforms are mainly formed by eruption-fed supercritical density flows associated with large explosive eruptions that lead to caldera collapses. A possible relationship between bedform size and magnitude of explosive eruption can be inferred, as testified to by the similarity in size between large-scale bedforms and associated calderas recognized around Macauley, Dakatua and Santorini edifices (Figs 2, 4 and Bell, 2011, respectively). Such large-scale bedforms appear to be absent on smaller calderas in submarine arc volcanoes, such as Ventotene (Casalbore *et al.*, 2016) or Vulcano edifices (Fig. 9). However, it is noteworthy that a large amount of volcaniclastic sediments can be delivered to the surrounding marine environment during smaller caldera forming events as well, promoting its successive dismantling through repeated slope failures and associated generation of small-scale bedforms, as for instance observed in the north-east part of Vulcano (Vul3 in Fig. 9). Here, a network of small gullies has largely dismantled the material infilling the submarine part of La Fossa Caldera, leading to the formation of the large Baia di Levante volcaniclastic fan downslope (Romagnoli *et al.*, 2012). Large-scale bedforms are often lacking on large calderas developed on basaltic volcanoes associated with Mid-Ocean Ridges or intraplate hotspot volcanism, whose formation is commonly related to syn- or post-eruption collapse following magma withdrawal (e.g., Fornari *et al.* 1984).

The second group of large-scale bedforms only develop in the deeper part of the submarine drainage networks affecting insular volcanoes and they can be unrelated to significant volcano-

tectonic events. The sediment-laden flows responsible for the formation of the bedforms can be triggered by several processes similar to what have been mentioned for the small-scale bedforms, including: (i) large hyperpycnal flows generated at subaerial rivers, especially on wide oceanic islands where well-developed subaerial drainage can develop, such as at Madeira (MA4 in Figs 3EMS and 14; Quartau *et al.*, 2018) or La Reunion islands (Sisavath *et al.*, 2011; Mazuel *et al.*, 2016); (ii) retrogressive slope failures occurring along the sidewalls and headwall of submarine channels. Most of these channels indent the insular shelf edge, where a significant amount of volcaniclastic deposits can be stored during highstand and transgressive system tracts and successively remobilized downslope (especially during lowstand periods), as observed at the Aeolian, Madeira (MA1, MA2, MA3 in Fig. 3EMS) and Azores archipelagos (Casalbore *et al.*, 2017b; Quartau *et al.*, 2012; 2014; 2015).

CONCLUSIONS

The comparison of bedform fields along the submarine flanks of several insular volcanoes has provided insights into their size distribution and controlling factors in a range of different geodynamic settings, morpho-structural evolution, volcanic and oceanographic regimes. The data herein indicate that a previously identified spatial gap in wavelength/wave height ratio may be an artifact of data resolution, and is not a true gap in the natural world. Therefore, the authors recommend the analysis of ancillary data (side scan sonar images, seismic profiles and AUV mounted bathymetry) coupled with a re-processing or new collection of high-resolution multibeam bathymetry along the middle and lower part of volcanic flanks to verify the possible occurrence of further examples of bedforms that fill this spatial gap. However, this work has identified a general distinction between small-scale bedforms (wavelengths of tens/hundreds of metres and wave heights of some metres) and large-scale bedforms (wavelengths of hundreds/thousands of metres and wave height up to hundreds of metres) (Fig. 14). In both cases, the bedforms are associated with major sediment sources and slope gradients play a key role in their development; with a maximum threshold of 15° and 8° (mainly between 3° to 5°) for small-scale and large-scale bedforms, respectively. Specifically, small-scale bedforms are mainly found in confined settings, i.e. the thalweg of shallow and flat-bottomed channels that carve the shelf surrounding volcanic islands. These small-scale bedforms are interpreted as the result of cyclic erosional–depositional processes associated with density flows that fluctuate between supercritical and subcritical modes, similar to the bedforms observed in active channels and prodeltas elsewhere. The flows are related

to a combination of volcanic and non-volcanic processes, among which sudden flood discharge or slope failures are the most common. For small-scale bedforms, the authors recommend performing repeated multibeam surveys to monitor their morphological evolution, because they can provide identification of their development and associated triggering mechanisms.

The interpretation of large-scale bedforms is more challenging, because they can be related to seafloor displacement induced by slope failures or cyclic erosional–depositional processes associated with density currents. Even if some morphological criteria are proposed to distinguish between these two types of bedforms (slope gradients, degree of confinement within landslide scars or downslope occurrence of compressional features or along-slope change in bedforms geometry), the authors recommend the use of seismic profiling and core data to better constrain their internal geometry and prevent erroneous interpretations. Large-scale bedforms generated by density currents occur both in confined and unconfined settings and they are often associated with main volcano-tectonic events, such as large flank or caldera collapses. Alternatively, large-scale bedforms can be observed on lower volcanic flanks at or close to marked breaks-in-slope (from 20° to 30° to values of a few degrees), often matching a change from confined to unconfined settings. Such 'breaks in slope' favour the formation of hydraulic jumps in large supercritical sediment-laden flows sourced from large depressions left by flank collapses, landslide scars affecting the insular shelf edge or reworking of caldera infilling. Data also show that the aspect (H/L) ratio of the bedforms (a parameter commonly used for their characterization) is generally scattered, but its range varies among the different edifices and/or in correspondence of abrupt morphological changes, suggesting that underlying morpho-structural controls may control the nature and dimensions of the bedforms.

In summary, the results of this study show that erosional–depositional bedforms are a common geomorphic feature observed in marine volcaniclastic settings, and their morphometric characterization provides insights into the associated density flows and more generally on the transfer of sediments from the tip to the base of the insular volcanoes. These inferences can be useful also to assess the geohazard associated with large turbidity or eruption-fed pyroclastic flows generated at volcanic islands and offshore areas, which can destructively impact offshore infrastructure.

ACKNOWLEDGEMENTS

We would like to thank the New Zealand National Institute of Water and Atmospheric Research (NIWA) for providing access to the Macauley Volcano dataset. Dr Gary Hoffman, Dr Eli Silver and Dr Phil Leat are thanked for making their bathymetry datasets of the South Sandwich Islands and New Britain publicly available. EP was supported by a Leverhulme Early Career Fellowship (ECF-2018-267). MC was supported by NERC CLASS project (grant number NE/R015953/1). DPC-INGV and MaGIC (Marine Geohazards Along the Italian Coast) projects are gratefully acknowledged for providing funding for data acquisition around Aeolian Islands as well as ship-time provided by National Research Council of Italy aboard *R/Vs Urania*, *Thetis* and *Minerva 1*. Officials and crews of these vessels are gratefully acknowledged along with the researchers and students taking part in the surveys. Multibeam data from Madeira archipelago was provided by the SEDMAR program funded by Instituto Hidrográfico. The Associate Editor Alexandre Normandeau, Katherine L. Maier and two anonymous reviewers are gratefully acknowledged for their useful comments and suggestions.

DATA AVAILABILITY STATEMENT

The morphometric data that support the findings of this study are available from the corresponding author, DC, upon reasonable request.

REFERENCES

Babonneau, N., Delacourt, C., Cancouët, R., Sisavath, E., Bachèlery, P., Mazuel, A., Jorry, S.J., Deschamps, A., Ammann, J., Villeneuve, N. (2013) Direct sediment transfer from land to deep-sea: insights into shallow multibeam bathymetry at La Réunion Island. *Mar Geol*, **346,** 47–57

Baioni, D. (2011) Human activity and damaging landslides and floods on Madeira Island. *Nat. Hazards Earth Syst. Sci*. **11,** 3035-3046**.**

Barker, S.J., Wilson, C.J.N., Baker, J.A., Millet, M.-A., Rotella, M.D., Wright, I.C., Wysoczanski, R.J. (2012). Geochemistry and petrogenesis of silicic magmas in the intra-oceanic Kermadec arc. J Petrol, **54**, 351-391.

Bell, K.L.C. (2011). On the origin of submarine sediment features in the southern Aegean Sea. Ph.D. thesis. University of Rhode Island

Blake, D.H., Bleeker, P. (1970) Volcanoes of the Cape Hoskins area, New Britain, territory of Papua and New Guinea. *Bulletin Volcanologique* **34**, 385-405.

Bosman, A., Casalbore, D., Romagnoli, C., & Chiocci, F. L. (2014). Formation of an 'a'ā lava delta: insights from time-lapse multibeam bathymetry and direct observations during the Stromboli 2007 eruption. *Bull Volcanol*, **76**(7), 838.

Boudon, G., Le Friant, A., Komorowski, J.-C., Deplus, C., Semet, M. (2007) Volcano flank instability in the Lesser Antilles Arc: diversity of scale, processes, and temporal recurrence. *J. Geophys. Res.* **112**, B08205. doi:10.1029/2006JB004674.

Bull, S., Cartwright, J., Huuse, M. (2009). A review of kinematic indicators from mass-transport complexes using 3D seismic data. *Marine and Petroleum Geology*, **26(7)**, 1132-1151.

Carey, S. (2000) Volcaniclastic sedimentation around island arcs. In: *Encyclopedia of volcanoes* (Ed. H. Sigurdsson). Academic Press, San Diego, pp. 627–642.

Carter, L., Gavey, R., Talling, P. J., Liu, J. T. (2014). Insights into submarine geohazards frombreaks in subsea telecommunication cables. *Oceanography* **27**, 58–67. doi: 10.5670/oceanog.2014.40

Cartigny, M.J.B., Postma, G., van den Berg, J.H., Mastbergen, D.R. (2011) A comparative study of sediment waves and cyclic steps based on geometries, internal structures and numerical modeling. *Mar Geol* **280**, 40-56.

Cartigny, M.J., Ventra, D., Postma, G., van Den Berg, J.H. (2014). Morphodynamics and sedimentary structures of bedforms under supercritical-flow conditions: new insights from flume experiments. *Sedimentology*, **61(3)**, 712-748.

Casalbore, D. (2018) Volcanic islands and seamounts. In: *Submarine Geomorphology*. Springer, Cham, 333-347.

Casalbore, D, Bosman, A, Romagnoli, C, Chiocci, FL (2013) Small-scale crescent-shaped bedforms in submarine volcanic setting: examples from Stromboli and Salina island (Italy). *GeoActa*, **12**, 37-45.

Casalbore, D., Romagnoli, C., Bosman, A., Chiocci, F.L. (2014). Large-scale seafloor waveforms on the flanks of insular volcanoes (Aeolian Archipelago, Italy), with inferences about their origin. *Mar. Geol.* **355**, 318–329.doi: 10.1016/j.margeo.2014.06.007

Casalbore, D., Romagnoli, C., Pimentel, A., Quartau, R., Casas, D., Ercilla, G., Hipolito, A., Sposato, A., Chiocci, F.L. (2015) Volcanic, tectonic and mass-wasting processes offshoreTerceira island (Azores) revealed by high-resolution seafloor mapping. *Bull. Volcanol*., **77** (3).

Casalbore, D., Bosman, A., Martorelli, E., Sposato, F.L., Chiocci, F.L. (2016) Mass wasting features on the submarine flanks of Ventotene volcanic edifice (Tyrrhenian Sea, Italy). In: *Submarine Mass Movements and Their Consequences* (Eds Krastel, *et al.*), **37**, 285–293.

Casalbore, D., Bosman, A., Romagnoli, C., Chiocci, F. L. (2017a) Small-scale bedforms generated by gravity flows in the Aeolian Islands. In *Atlas of Bedforms in the Western Mediterranean*. Springer, Cham pp. 287-292.

Casalbore, D, Falese, F, Martorelli, E, Romagnoli, C, Chiocci, FL (2017b) Submarine depositional terraces in the Tyrrhenian sea as a proxy for paleo-sea level reconstruction: problems and perspective. *Quat Int* **439**,169–180.

Casalbore, D., Romagnoli, C., Bosman, A., Anzidei, M., Chiocci, F. L. (2018). Coastal hazard due to submarine canyons in active insular volcanoes: examples from Lipari Island (southern Tyrrhenian Sea). *J Coast Conserv*, **22**(5), 989-999.

Chadwick Jr., W.W., Cashman, K.V., Embley, R.W., Matsumoto, H., Dziak, R.P., de Ronde, C.E.J., Lau, T.K., Deardorff, N.D., Merle, S.G. (2008) Direct video and hydrophone observations of submarine explosive eruptions at NW Rota-1 volcano, Mariana arc. *Journal of Geophysical Research*: *Solid Earth* 113.

Chen, J. K., Taylor, F. W., Edwards, R. L., Cheng, H., Burr, G.S. (1995). Recent emerged reef terraces of the Yenkahe resurgent block, Tanna, Vanuatu: implications for volcanic, landslide and tsunami hazards. *The Journal of Geology*, **103(5)**, 577-590.

Chiocci, F.L., Casalbore, D. (2017). Unexpected fast rate of morphological evolution of geologically-active continental margins during Quaternary: Examples from selected areas in the Italian seas. *Marine and Petroleum Geology*, **82**, 154-162.

Chiocci, F.L., Romagnoli, C., (2004). Terrazzi deposizionali sommersi nelle Isole Eolie. *Memorie Descrittive della Carta Geologica d' Italia* **58**, 81–114.

Chiocci, FL, Romagnoli, C, Tommasi, P, Bosman, A (2008) Stromboli 2002 tsunamigenic submarine slide: characteristics and possible failure mechanisms. *J Geophys Res,* **113**, B10102.

Chiocci FL, Romagnoli C, CasalboreD et al (2013) Bathy-morphological setting of Terceira island (Azores) after the FAIVI cruise. *J Maps* **9**, 590–595.

Clare, M. A., Clarke, J. H., Talling, P. J., Cartigny, M. J. B., and Pratomo, D. G. (2016). Preconditioning and triggering of offshore slope failures and turbidity currents revealed by most detailed monitoring yet at a fjordhead delta. *Earth Planetary Sci. Lett.* **450**, 208–220. doi: 10.1016/j.epsl.2016.06.021

Clare, MA, Le Bas, T, Price, DM, Hunt, JE, Sear, D, Cartigny, MJB, Vellinga, A, Symons W, Firth C, Cronin, S (2018) Complex and Cascading Triggering of Submarine Landslides and Turbidity Currents at mVolcanic Islands Revealed From mIntegration of High-Resolution Onshore and Offshore Surveys. *Front. Earth Sci.,* **6**,223. mdoi: 10.3389/feart.2018.00223

Coombs, M.L., White, S.M., Scholl, D.W. (2007). Massive edifice failure at Aleutian Arc volcanoes. *Earth Planet. Sci. Lett.* doi:10.1016/j.epsl.2007.01.030.

Covault, J.A., Kostic, S., Paull, C.K., Ryan, H.F. and Fildani, A. (2014). Submarine channel initiation, filling and maintenance from sea-floor geomorphology and morphodynamic modelling of cyclic steps. *Sedimentology*, **61(4)**, 1031-1054.

Covault, J.A., Kostic, S., Paull, C.K., Sylvester, Z. and Fildani, A. (2017). Cyclic steps and related supercritical bedforms: building blocks of deep-water depositional systems, western North America. *Marine Geology*, **393**, 4-20.

Dietrich, P., Ghienne, J. F., Normandeau, A., Lajeunesse, P. (2016). Upslope-migrating bedforms in a proglacial sandur delta: cyclic steps from river-derived underflows?. *Journal of Sedimentary Research*, **86(1)**, 112-122.

Ercilla, G., Alonso, B., Wynn, R.B., Baraza, J. (2002). Turbidity current sediment waves on irregular slopes: observations from the Orinoco sediment–wave field. *Mar Geol*, **192(1-3)**, 171-187.

Firth, C. W., Handley, H. K., Cronin, S. J., Turner, S. P. (2014). The eruptive history and chemical stratigraphy of a post-caldera, steady-state volcano: Yasur, Vanuatu. *Bull of Volcanol* **76(7),** 837.

Firth, C. W., Cronin, S. J., Turner, S. P., Handley, H. K., Gaildry, C., Smith, I. (2015). Dynamics and pre-eruptive conditions of catastrophic, ignimbrite-producing eruptions from the Yenkahe Caldera, Vanuatu. *J Volcanol Geoth Res*, **308**, 39-60.

Fricke, A.T., Sheets, B.A., Nittrouer, C.A., Allison, M. A., Ogston, A.S. (2015). An examination of Froude-supercritical flows and cyclic steps on a subaqueous lacustrine delta, Lake Chelan, Washington, USA. *Journal of Sedimentary Research*, **85(7)**, 754-767.

Fornari, DJ, Ryan, WBF, Fox, PJ (1984) The evolution of craters and calderas on young seamounts: insights from sea MARC1 and SEABEAM sonar surveys of a small seamount group near the axis of the East Pacific Rise at 108N. *J Geophys Res* **89**,11069–11083

Gardner, J.V. (2010) The West Mariana Ridge, western Pacific Ocean: geomorphology and processes from new multibeam data. *Geol. Soc. Am. Bull.*, **122**, 1378–1388.

Geldmacher, J., van den Bogaard, P., Hoernle, K., Schmincke, H.-U. (2000) The 40Ar/39Ar age dating of the Madeira Archipelago and hotspot track (eastern North Atlantic). *Geochem. Geophys. Geosyst.* **1**, 1-26.

Geldmacher, J., Hoernle, K., van den Bogaard, P., Zankl, G., Garbe-Schonberg, D. (2001) Earlier history of the >= 70-Ma-old Canary hotspot based on the temporal and geochemical evolution of the Selvagen Archipelago and neighboring seamounts in the eastern North Atlantic. *J. Volcanol. Geotherm. Res.* **111**, 55-87.

Hage, S., Cartigny, M. J., Clare, M. A., Sumner, E. J., Vendettuoli, D., Hughes Clarke, J. E., *et al.* (2018). How to recognize crescentic bedforms formed by supercritical turbidity currents in the geologic record: insights from active submarine channels. *Geology* **46**, 563–566. doi: 10.1130/G40095.1.

Hage, S., Cartigny, M.J., Sumner, E.J., Clare, M.A., Hughes Clarke, J.E., Talling, P.J., Lintern, D.G., Simmons, S.M., Silva Jacinto, R., Vellinga, A.J. and Allin, J.R. (2019). Direct monitoring reveals initiation of turbidity currents from extremely dilute river plumes. *Geophysical Research Letters*, 6, 11,310–11,320.

Hampton, M.A., Lee, H.J., Locat, J. (1996) Submarine landslides. *Reviews of Geophysics* **34**, 33-59.

Hernández-Molina, F.J., Fernández-Salas, L.M., Lobo, F., Somoza, L., Díaz-del-Río, V., Dias, J.A. (2000). The infralittoral prograding wedge: a new large-scale progradational sedimentary body in shallow marine environments. *Geo-Marine Letters*, **20(2)**, 109-117.

Hoffmann, G., Silver, E., Day, S., Morgan, E., Driscoll, N., Orange, D. (2008) Sediment waves in the Bismarck volcanic arc, Papua New Guinea. *Geological Society of America Special Papers* **436**, 91-126.

Hoffmann, G., Silver, E., Day, S., Driscoll, N., Orange, D. (2011) Deformation versus deposition of sediment waves in the Bismarck Sea, Papua New Guinea. Mass-transport deposits in deepwater settings. *SEPM Spec Publ* **96**, 455-474.

Hughes Clarke, J. E. (2016). First wide-angle view of channelized turbidity currents links migrating cyclic steps to flow characteristics. *Nat Commun.* **7**,11896. doi: 10.1038/ncomms11896.

Kokelaar, P., Romagnoli, C. (1995). Sector collapse, sedimentation and clast population evolution at an active island-arc volcano: Stromboli, Italy. *Bulletin of Volcanology*, **57(4)**, 240-262.

Kostic, S. (2011). Modeling of submarine cyclic steps: Controls on their formation, migration, and architecture. *Geosphere*, **7(2)**, 294-304.

Kostic, S. (2014). Upper flow regime bedforms on levees and continental slopes: Turbidity current flow dynamics in response to fine-grained sediment waves. *Geosphere*, **10(6)**, 1094-1103.

Larter, R.D., Vanneste, L.E., Morris, P., Smythe, D.K. (2003) Structure and tectonic evolution of the South Sandwich arc. *Geological Society, London, Special Publications* **219**, 255-284.

Lee, H.J., Syvitski, J.P.M., Parker, G., Orange, D., Locat, J., Hutton, E.W.H., Imran, J. (2002) Distinguishing sediment waves from slope failure deposits: field examples, including the "Humboldt Slide" and modeling results. *Mar Geol* **192**, 79–104.

Leat, P.T., Smellie, J.L., Millar, I.L., Larter, R.D. (2003) Magmatism in the South Sandwich arc. *Geological Society, London, Special Publications* **219**, 285-313.

Leat, P.T., Tate, A.J., Tappin, D.R., Day, S.J., Owen, M.J. (2010) Growth and mass wasting of volcanic centers in the northern South Sandwich arc, South Atlantic, revealed by new multibeam mapping. *Mar Geol*, **275**, 110-126.

Li, J., Li, W., Alves, T. M., Rebesco, M., Zhan, W., Sun, J., Mitchell, N., Wu, S. (2019). Different origins of seafloor undulations in a submarine canyon system, northern South China Sea, based on their seismic character and relative location. *Mar Geol*, **413**, 99-111.

Lloyd, E.F., Nathan, S., Smith, I.E.M., Stewart, R.B. (1996) Volcanic history of Macauley Island, Kermadec Ridge, New Zealand. *Journal of Geology and Geophysics* **39**, 295-308.

Lowder, G.G., Carmichael, I.S.E. (1970) The volcanoes and caldera of Talasea, New Britain: geology and petrology. *Geological Society of America Bulletin* **81**, 17-38.

Lucchi, F., Keller, J., Tranne, C. A. (2013). Regional stratigraphic correlations across the Aeolian archipelago (southern Italy). In: *The Aeolian Islands Volcanoes* (Eds Lucchi, F., Peccerillo, A., Keller, J., Tranne, C.A., Rossi, P.L.). Geological Society, London. Memoirs, 37, pp. 56–81.

Mazuel, A., Sisavath, E., Babonneau, N., Jorry, S.J., Bachèlery, P., Delacourt, C. (2016) Turbidity current activity along the flanks of a volcanic edifice: the mafate volcaniclastic complex, La Réunion Island, Indian Ocean. *Sediment. Geol.* **335**, 34–50.

McGuire, W. J. (2006). Lateral collapse and tsunamigenic potential of marine volcanoes. *Geological Society, London, Special Publications*, **269**(1), 121-140.

Menard, H.W. (1956) Archipelagic aprons. *AAPG Bulletin* **40**, 2195–2210.

Merle, O., Brothelande, E., Lénat, J. F., Bachèlery, P., Garaébiti, E. (2013). A structural outline of the Yenkahe volcanic resurgent dome (Tanna Island, Vanuatu Arc, South Pacific). *J Volcanol Geoth Res*, **268**, 64-72.

Micallef, A., Mountjoy, J. J. (2011). A topographic signature of a hydrodynamic origin for submarine gullies. *Geology*, **39(2),** 115-118

Mitchell, N.C., Masson, D.G., Watts, A.B., Gee, M.J.R., Urgeles, R. (2002) The morphology of the submarine flanks of volcanic ocean islands. A comparative study of the Canary and Hawaiian hotspot islands. *J Volcanol Geoth Res*, **115**, 83–107.

Mitchell NC, Beir C, Rosin PL, Quartau R, Tempera F (2008) Lava penetrating water: submarine lava flows around the coasts of Pico Island, Azores. *Geochem Geophys Geosyst* , **9**, Q03024. doi:10.
1029/2007GC001725

Mulder, T, Syvitski, JPM (1995) Turbidity currents generated at mouths of rivers during exceptional discharges to the world oceans. *J Geol* **103**, 285–299.

Nairn, I.A., Scott, B.J. and Giggenbach, W.F. (1988). Yasur volcano investigations, Vanuatu, September 1988. *New Zealand Geological Survey Report*, G134, 74

Neall, V.E., Wallace, R.C., Torrence, R. (2008) The volcanic environment for 40,000 years of human occupation on the Willaumez Isthmus, West New Britain, Papua New Guinea. *J Volcanol Geoth Res* **176**, 330-343.

Newhall, C.G., Punongbayan, R.S. (1996) Fire and mud: Eruptions and lahars of Mount Pinatubo: Seattle, University of Washington Press, 1126 p.

Normandeau, A., Lajeunesse, P., Poiré, A. G., and Francus, P. (2016). Morphological expression of bedforms formed by supercritical sediment density flows on four fjord-lake deltas of the south-eastern Canadian Shield (Eastern Canada). *Sedimentology* **63**, 2106–2129. doi: 10.1111/sed.12298.

O'Grady, D.B., Syvitski, J.P.M, Pratson, L.F., Sarg, J.F. (2000) Categorizing the morphologic variability of siliciclastic passive continental margins. *Geology*, **28**, 207-210.

Omira, R., Quartau, R., Ramalho, R., Baptista, M.A., Mitchell, N.C. (2016) The tsunami effects of a large-scale flank collapse on a semi-enclosed basin: the Pico-S. Jorge channel in the Azores archipelago**.** In: *Plate Boundaries and Natural Hazards* (Eds. Duarte, J.C., Schellart, W.P.). John Wiley & Sons, Inc, New Jersey, pp. 271–287.

Paull, C.K., Caress, D.W., Ussler, W., III, Lundsten, E., and Thomas, H., (2008) Axial channel morphology fill and movement within submarine canyons off California**.** American Geophysical Union**,** Fall Meeting 2008, abs. OS54A-01

Paull, C.K., Ussler III,W., Caress, D.W., Lundsten, E., Barry, J., Covault, J.A., Maier, K.L., Xu, J.P., Augenstein, S. (2010) Origins of large crescent-shaped bedformswithin the axial channel of Monterey Canyon. *Geosphere* **6**, 755–774 **.**

Paull, C.K., Talling, P.J., Maier, K.L., Parsons, D., Xu, J., Caress, D.W., Gwiazda, R., Lundsten, E.M., Anderson, K., Barry, J.P. and Chaffey, M. (2018). Powerful turbidity currents driven by dense basal layers. *Nature communications*, **9(1),** 4114**.**

Pearce, J.A., Baker, P.E., Harvey, P.K., Luff, I.W. (1995) Geochemical evidence for subduction fluxes, mantle melting and fractional crystallization beneath the South Sandwich island arc. *Journal of Petrology* **36**, 1073-1109.

Pope, E. L., Talling, P. J., Carter, L., Clare, M. A., Hunt, J. E. (2017). Damaging sediment density flows triggered by tropical cyclones. *Earth Planet. Sci. Lett*., **458**, 161–169. doi: 10.1016/j.epsl.2016.10.046.

Pope, E.L., Jutzeler, M., Cartigny, M.J.B., Shreeve, J., Talling, P.J., Wright, I.C., Wysoczanski, R.J. (2018) Origin of spectacular fields of submarine sediment waves around volcanic islands. *Earth and Planetary Science Letters*, **493**, 12-24.

Postma, G., Cartigny, M.J. (2014). Supercritical and subcritical turbidity currents and their deposits—A synthesis. *Geology*, **42(11)**, 987-990.

Postma, G., Cartigny, M., Kleverlaan, K. (2009) Structureless, coarse-tail graded Bouma Ta formed by internal hydraulic jump of the turbidity current? *Sedimentary Geology* **219 (1–4)**, 1–6.

Quartau, R, Trenhaile, AS, Mitchell, NC, Tempera, F (2010) Development of volcanic insular shelves: Insights from observations and modelling of Faial Island in the Azores Archipelago. *Mar Geol* **275**, 66–83.

Quartau, R, Tempera, F, Mitchell, NC, Pinheiro, LM, Duarte, H, Brito, PO, Bates, R, Monteiro, JH (2012) Morphology of the Faial Island shelf (Azores): the interplay between volcanic, erosional, depositional, tectonic and mass-wasting processes. *Geochem Geophys Geosy* **13**, Q04012.

Quartau, R., Hipólito, A., Romagnoli, C., Casalbore, D., Madeira, J., Tempera, F., Roque, C., Chiocci, F.L. (2014) The morphology of insular shelves as a key for understanding the geological evolution of volcanic islands: insights from Terceira Island (Azores). *Geochem Geophys Geosy* **15**,1801–1826.

Quartau, R., Madeira, J., Mitchell, N. C., Tempera, F., Silva, P. F., & Brandão, F. (2015). The insular shelves of the Faial-Pico Ridge (Azores archipelago): A morphological record of its evolution. *Geochem, Geophys, Geosy*, **16**(5), 1401-1420.

Quartau, R., Ramalho, R.S., Madeira, J., Santos, R., Rodrigues, A., Roque, C., Carrara, G., da Silveira, A.B. (2018) Gravitational, erosional and depositional processes on volcanic ocean islands: Insights from the submarine morphology of Madeira Archipelago. *Earth and Planetary Science Letters*, **482**, 288-299.

Ramalho, R. S., Quartau, R., Trenhaile, A. S., Mitchell, N. C., Woodroffe, C. D., Avila, S. P. (2013). Coastal evolution on volcanic oceanic islands: A complex interplay between volcanism, erosion, sedimentation, sea-level change and biogenic production. *Earth-Science Reviews*, **127**, 140-170.

Ramalho, R.S., Brum da Silveira, A., Fonseca, P., Madeira, J., Cosca, M., Cachão, M., Fonseca, M., Prada, S. (2015)**.** The emergence of volcanic oceanic islands on a slow-moving plate: the example of Madeira Island, NE Atlantic. *Geochem. Geophys. Geosyst.* **16,** 522–537.

Ricchi, A., Quartau, R., Ramalho, R. S., Romagnoli, C., Casalbore, D., da Cruz, J. V., Fradique, C., Vinhas, A. (2018). Marine terrace development on reefless volcanic islands: New insights from high-resolution marine geophysical data offshore Santa Maria Island (Azores Archipelago). *Mar Geol* **406,** 42-56.

Romagnoli, C., Mancini, F., & Brunelli, R. (2006). Historical shoreline changes at an active island volcano: Stromboli, Italy. *Journal of Coastal Research*, 739-749.

Romagnoli, C., Casalbore, D., Chiocci, F.L. (2012) La Fossa Caldera breaching and submarine erosion (Vulcano island, Italy). *Mar. Geol* **303–306**, 87–98.

Romagnoli, C, Casalbore, D, Bortoluzzi, G, Bosman, A, Chiocci, FL, D'Oriano F, Gamberi, F, Ligi, M, Marani, M (2013a) Bathymorphological setting of the Aeolian islands. In: *The Aeolian Islands Volcanoes* (Eds Lucchi F, Peccerillo A, Keller J, Tranne CA, Rossi PL), vol 37. Geological Society, London, Memoirs, pp 27–36.

Romagnoli, C, Casalbore, D, Bosman, A, Braga, R, Chiocci, FL (2013b) Submarine structure of Vulcano volcano (Aeolian islands) revealed by high-resolution bathymetry and seismo-acoustic data. *Mar Geol* **338**, 30–45

Romagnoli, C., Casalbore, D., Ricchi, A., Lucchi, F., Quartau, R., Bosman, A., Tranne, C.A., Chiocci, F. L. (2018). Morpho-bathymetric and seismo-stratigraphic analysis of the insular shelf of Salina (Aeolian archipelago) to unveil its Late-Quaternary geological evolution. *Mar Geol*, **395**, 133-151.

Romagnoli, C., Kokelaar, P., Casalbore, D., Chiocci, F.L. (2009a) Lateral collapses and active sedimentary processes on the northwestern flank of Stromboli volcano. *Mar Geol* **265**, 101–119.

Rosi, M., Bertagnini, A., Landi, P. (2000) Onset of persistent activity at Stromboli volcano (Italy). *Bull Volcanol* **62**, 294–300.

Santos, R., Quartau, R., da Silveira, A. B., Ramalho, R., & Rodrigues, A. (2019). Gravitational, erosional, sedimentary and volcanic processes on the submarine environment of Selvagens Islands (Madeira Archipelago, Portugal). *Mar Geol*., **415**, 105945.

Schlager, W. and Camber, O. (1986). Submarine slope angles, drowning unconformities, and self-erosion of limestone escarpments. *Geology*, **14(9)**, 762-765.

Schmidt, R., Schmincke, H.-U. (2002) From seamount to oceanic island, Porto Santo, central East-Atlantic. *Int. J. Earth Sci.* (Geol. Rundsch) **91**, 594-614.

Schwarz, S., Klügel, A., van den Bogaard, P., Geldmacher, J. (2005) Internal structure and evolution of a volcanic rift system in the eastern North Atlantic: the Desertas rift zone, Madeira archipelago. J. *Volcanol. Geotherm. Res*. **141**, 123-155

Shane, P., Wright, I.C. (2011) Late Quaternary tephra layers around Raoul and Macauley Islands, Kermadec Arc: implications for volcanic sources, explosive volcanism and tephrochronology. *J Quaternary Sci* **26**, 422-432.

Silver, E.A., Abbott, L.D., Kirchoff-Stein, K.S., Reed, D.L., Bernstein-Taylor, B., Hilyard, D. (1991) Collision propagation in Papua New Guinea and the Solomon Sea. *Tectonics* **10**, 863-874.

Silver, E., Day, S., Ward, S., Hoffmann, G., Llanes, P., Driscoll, N., Appelgate, B., Saunders, S. (2009) Volcano collapse and tsunami generation in the Bismarck volcanic arc, Papua New Guinea. *Journal of Volcanology and Geothermal Research*, **186**, 210-222.

Sisavath, E., Babonneau, N., Saint-ange, F., Bachèlery, P., Jorry, S.J., Deplus, C., De Voogd, B.,Savoye, B. (2011) Morphology and sedimentary architecture of a modern volcaniclastic turbidite system: the Cilaos fan, offshore La Réunion Island. *Mar Geol*, **288**, 1–17.

Slootman, A., Cartigny, M. J. (2019). Cyclic steps: Review and aggradation-based classification. *Earth-Science Reviews*, 102949.

Smith, I.E.M., Stewart, R.B., Price, R.C. (2003) The petrology of a large intra-oceanic silicic eruption: the Sandy Bay Tephra, Kermadec Arc, Southwest Pacific. *J Volcanol Geoth Res* **124**, 173-194.

Spinewine, B., Sequeiros, O.E., Garcia, M.H., Beaubouef, R.T., Sun, T., Savoye, B. (2009) Experiments on wedge-shaped deep-sea sedimentary deposits in minibasins and/or on channel levees emplaced by turbidity currents. Part II. Morphodynamic evolution of the wedge and of the associated bedforms. *Journal of Sedimentary Research* **79 (8)**, 608.

Symons, W.O., Sumner, E.J., Talling, P.J., Cartigny, M.J.B., Clare, M.A. (2016) Large-scale sediment waves and scours on the modern seafloor and their implications for the prevalence of supercritical flows. *Mar. Geol.* **371**, 130–148.

Tappin, D.R., Watts, P., Grilli, S.T. (2008). The Papua New Guinea tsunami of 17 July 1998: anatomy of a catastrophic event. *Natural Hazards and Earth System Science*, **8**(2), 243-266.

Vendettuoli, D., Clare, M.A., Clarke, J.H., Vellinga, A., Hizzet, J., Hage, S., Cartigny, M.J.B., Talling, P.J., Waltham, D., Hubbard, S.M. and Stacey, C. (2019). Daily bathymetric surveys document how stratigraphy is built and its extreme incompleteness in submarine channels. *Earth and Planetary Science Letters*, **515**, 231-247.

Ventura, G. (2013). Kinematics of the Aeolian volcanism (Southern Tyrrhenian Sea) from geophysical and geological data. In: *The Aeolian Islands Volcanoes* (Eds Lucchi F, Peccerillo A, Keller J, Tranne CA, Rossi PL), vol 37. Geological Society, London, Memoirs, pp 3-11.

Williams, R., Rowley, P., Garthwaite, M.C. (2019). Reconstructing the Anak Krakatau flank collapse that caused the December 2018 Indonesian tsunami. *Geology*, **47(10)**, 973-976.

Wright, I.C., Worthington, T.J., Gamble, J.A. (2006) New multibeam mapping and geochemistry of the 30–35 S sector, and overview, of southern Kermadec arc volcanism. *J Volcanol Geoth Res*, **149**, 263-296.

Williams *et al.*, 2019

Wynn, R.B., Masson, D.G., Stow, D.A.V., Weaver, P.P.E. (2000) Turbidity current sediment waves on the submarine slopes of the western Canary Islands. *Mar Geol*, **163**, 185–198.

Wynn, R.B., Piper, D.J.W., Gee, M.J.R. (2002) Generation and migration of coarse-grained sediment waves in turbidity current channels and channel–lobe transition zones. *Mar Geol* **192**, 59-78.

Zhong, G., Cartigny, M. J., Kuang, Z., Wang, L. (2015). Cyclic steps along the South Taiwan Shoal and West Penghu submarine canyons on the northeastern continental slope of the South China Sea. *GSA Bulletin*, 1**27(5-6)**, 804-824.

Additional References (ESM)

Bosman, A., Casalbore, D., Anzidei, M., Muccini, F., Carmisciano, C., Chiocci, F.L. (2015) *Ann. Geophys.*, **58**, S0218. doi:10.4401/ag-6746.

Calder, B.R., Mayer, L.A. (2003). Automatic processing of high-rate, high-density multibeam echosounder data. *Geochemistry, Geophysics, Geosystems*, 4(6).

Casalbore, D., Romagnoli, C., Chiocci, F., Frezza, V. (2010) Morphosedimentary characteristics

of the volcanic apron around Stromboli volcano. *Mar Geol* **269** (3–4), 132–148.

Romagnoli, C., Casalbore, D., Chiocci, F.L., Bosman, A. (2009b) Offshore evidence of largescale lateral collapse on the eastern flank of Stromboli, Italy, due to structurally controlled, bi-lateral flank instability. *Mar Geol* **262**, 1–13.

Rothwell, R. G., Hoogakker, B., Thomson, J., Croudace, I. W., & Frenz, M. (2006). Turbidite emplacement on the southern Balearic Abyssal Plain (western Mediterranean Sea) during Marine Isotope Stages 1–3: an application of ITRAX XRF scanning of sediment cores to lithostratigraphic analysis. *Geological Society, London, Special Publications*, **267**(1), 79-98.

Tate, A.J., Leat, P.T. (2007) RRS James Clark Ross JR168 cruise report: swath bathymetry South Sandwich Islands, British Antarctic Survey Reprot ES6/1/2007/1, https://www.bodc.ac.uk/data/information_and_inventories/cruise_inventory/report/9079.

FIGURE CAPTIONS

Figure 1 Location of the study-areas presented in this paper. Bathymetry was downloaded from GEBCO and EMODNET website

Figure 2. (A) Map of bedforms surrounding Macauley Volcano. Bedform fields (enclosed by solid black lines) and associated bathymetric profilers (A' to F', dashed black lines) included in Table 1 are indicated. (B) Un-interpreted seismic profile (location in Fig. 2A) perpendicular to the expected direction of flow of an eruption-fed sediment density flow. (C) Trace interpretation of seismic reflectors within the bedforms. The green line represents an interpreted unconformity within the bedforms. (D) and (E) Bathymetric profiles along the centre of the bedform fields identified in (A) and described in Table 1.

Figure 3. (A) Map of bedforms surrounding Zavodovski Volcano. Bedform fields (enclosed by solid black lines) included in Table 1 are indicated. (B) to (D) Bathymetric profiles and slope gradients along the profiles of the bedform fields identified in (A).

Figure 4. (A) Map of bedforms surrounding Dakataua Caldera. Bedform fields (enclosed by solid black lines) included in Table 1 are indicated. (B) to (C) Bathymetric profiles and slope gradients along the profiles of the bedform fields identified in (A).

Figure 5. (A) Map of bedforms on the seafloor of Kimbe Bay. Bedform field KB (enclosed by solid black lines) is included in Table 1. (B) Bathymetric profile and slope gradient along profile A – A' in (A).

Figure 6 (A) Shaded relief map of the Piscità channel (bathymetry was collected in 2013), where the bedforms field Str4 (location in Fig. 1 and 1ESM) is recognizable; bathymetric section A–A' (dark line) and slope gradients (grey-line) are shown on the right. (B) Difference map between 2002 and 2003 bathymetries collected before and after the Stromboli 2002 eruption and tsunamigenic landslide, evidencing a main migration of bedforms on the eastern side of the channel. Bathymetric profile B–B' is shown on the upper right panel, evidencing an upslope migration between 2002 (blue line) and 2003 (red line) bathymetries. (C) Difference map between 2013 and 2015 bathymetries collected before and after the 2014 Stromboli eruption, showing the migration of the bedforms mainly on the eastern side of the channel. Bathymetric profile C–C' is shown on the upper right panel, evidencing the formation of a new coaxial train of bedforms between 2013 (green line) and 2015 (violet line) bathymetries.

Figure 7 Shaded relief map of the Northern Salina channel, where the bedforms field Sal1 (location in Fig. 1 and 1 ESM) is recognizable; on the right, bathymetric sections (dark line) and slope gradients (grey-line) extracted from the digital elevation model (DEM) are shown.

Figure 8 Shaded relief map of the eastern flank of Salina, where the bedforms field Sal2 (location in Fig. 1 and 1 ESM) is recognizable; below, bathymetric sections (dark line) and slope gradients (grey-line) extracted from the digital elevation model (DEM) are shown.

Figure 9 Shaded relief map of the northern flank of Vulcano, where the bedforms fields Vul2 and Vul3 (location in Fig. 1 and 1ESM) are recognizable in the north-west and north-east flank, respectively; below, bathymetric sections (dark line) and slope gradients (grey-line) extracted from the digital elevation model (DEM) are shown.

Figure 10 Shaded relief map to illustrate bedform fields (Vn1 to Vn4) offshore Tanna Island, Vanuatu including (A) overview and detailed close-up views (B) (C) and (E) showing small-scale bedforms. Profiles in (D) and (F) illustrate the variability in scale of bedforms from proximal to distal, as well as in response to topographic changes seaward of the interpreted former caldera collapse.

Figure 11 Shaded relief map of the eastern side of Desertas and southern side of Porto Santo where the bedforms MA1 and MA2 were identified. DS1 to DS4 are bathymetric profiles and slope gradients along the profiles of the bedform fields identified in the upper image; profile PS1 is shown in Fig. 12. Solid blue lines represent shelf edge scars. Location in Fig. 1 and Fig. 2 ESM.

Figure 12 Shaded relief map of the northern side of Porto Santo where the bedforms MA3 were identified. PS1 to PS5 are bathymetric profiles and slope gradients along the profiles of the bedform fields identified in the upper image. Solid blue lines represent shelf edge scars. Location of PS1 is shown in Fig. 11

Figure 13 Shaded relief map of Selvagens where the bedforms SEL1 to SEL4 were identified. SV1 to SV5 are bathymetric profiles and slope gradients along the profiles of the bedform fields identified in the upper image.

Figure 14 Sketch summarising in the upper part the main morphological features and setting of erosive–depositional bedforms in marine volcaniclastic areas described in this work; MBES: multibeam echosounder. In the lower part of the sketch, the main preconditioning/triggering factors for the development of the bedforms are also shown; the different acronyms are referred to the bedform fields described in the main text: Str: Stromboli, Sal: Salina; Vul: Vulcano; Pan: Panarea; MA: Madeira; SEL: Selvagens; MC: Maucaley.

Figure 15 (A) Plot of wave height versus wavelength for all the recognized bedforms. Boundaries of H/L ratio for the large-scale (B) and small-scale (C) bedform fields recognized in the different case-studies. Note that for small-scale bedform fields in (C), outliers are not shown to improve the readability of the graph. The dashed lines are referred to 1:10, 1:25, 1:50, 1:100 H/L values.

Figure 1 ESM – Shaded relief map of the five insular volcanoes making up the central and eastern sectors of the Aeolian Archipelago, with the location of the large-scale (magenta areas; from Casalbore *et al.*, 2014) and small-scale bedform fields described in this study (light-blue areas, see also Figs 6 to 9). The main submarine morphological features useful to understand the genesis of the bedforms are also drawn, such as the main landslide scars (red lines), drainage network (blue line), insular shelf edge (green line) and prevalent littoral drift around the northern part of Stromboli island (magenta line); SdF: Sciara del Fuoco. The inset shows the regional setting of the area, where triangles represent submarine seamounts also belonging to the Aeolian Arc.

Figure 2 ESM – Shaded relief map of subaerial and submarine part of Madeira, Porto Santo and Desertas islands with bedform fields identified MA1 to MA5.

Figure 3 ESM – Shaded relief map of the northern side of Madeira where the bedforms MA4 and MA5 were identified. Solid blue lines represent shelf edge scars. MAD1 to MAD4 are bathymetric profiles and slope gradients along the profiles of the bedform fields identified in the upper image.

Table 1 Main morphometric characteristics of the recognized bedforms. Note that the slope range is referred to maximum and minimum values of the slope gradients measured in the bedforms field by deleting the local effect of the bedforms. L, H and L.E. are wavelength, wave height and lateral extent, respectively; min: minimum, max: maximum, med: median. Negative values shown in brackets for stoss–side are referred to the maximum slope gradients measured in the cases where the stoss–side is sloping upslope instead than downslope.

ID*	Location	Area km^2	Depth range m	Slope range °	L (min) m	L (max) m	L (med) m	H (min) m	H (max) m	H (med) m	L.E. (min) m	L.E. (max) m	L.E. (med) m	Crestline shape	Cross–section	Stoss–side (max slope angle) °	Lee side (max slope angle) °
MC1	Macauley	>320	650 – 1700	3.52 – 0.99	250	1500	620	5	140	38	7250	27000	17000	Convex	Downslope asymmetrical	13.7	24.3
MC2	Macauley	220	630 – 1900	5.52 – 1.98	220	1650	650	5	160	40	7800	12250	9600	Convex	Downslope asymmetrical	16.2	22.7
MC3	Macauley	>120	750 – 1650	3.45 – 1.95	525	1250	850	17	200	90	2600	9700	7800	Cinuous/ Linear	Symmetrical	14.6	24.0
MC4	Macauley	>81	450 – 1650	3.16 – 2.66	350	1350	750	13	140	63	2600	4250	3850	Cinuous/ Linear	Symmetrical	15.6	21.2
MC5	Macauley	>279	600 – 3300	3.36 – 3.36	350	2450	1237	5	75	31	800	20100	9100	Cinuous	Symmetrical	21.2	28.2
MC6	Macauley	65	350 – 1150	4.59 – 2.99	125	1254	475	5	90	37	1900	7400	3200	Concave upslope/ Linear downslope	Upslope Asymmetrical (upslope) Symmetrical (downslope)	13.3	18.8
Zd1	Zavodovski	368	160 – 2130	4.06 – 1.97	380	2800	1037	5	144	54	1450	16500	8200	Convex/ Linear	Downslope asymmetrical	9.9	9.9

Zd2	Zavodovski	186	400 – 2800	3 –2.54	190	1900	663	8	164	63	1700	3150	2100	Concave/ Linear	Downslope asymmetrical Upslope asymmetrical	8.1	8.5
Zd3	Zavodovski	>313	370 – 2600	3.96 – 2.22	285	2957	1437	24	175	108	2300	12600	10100	Linear	Downslope asymmetrical	7.84	11.1
DC2	Dakataua Caldera	520	1600 – 2100	1.23 – 0.66	820	2860	1898	10	115	40	5900	28500	20200	Convex	Downslope asymmetrical Upslope asymmetrical	5.1	9.9
DC1	Dakataua Caldera	554	1450 – 2000	2.33 –0.3	384	3500	990	5	92	21	6600	19800	15000	Sinuous/ Linear	Downslope asymmetrical Upslope asymmetrical	3.66	7.66
KB	Kimbe Bay	700	1500 – 2200	1.1 –0.4	494	3400	1430	7	84	35	7800	21700	13800	Convex	Downslope asymmetrical Upslope asymmetrical	4.77	10.14
Str1	Stromboli SE	15	1500– 1700	5 –2	60	400	173	5	20	3.1	70	800	220	Sinuous to arcuate	Mostly downslope asymmetrical	3.0 (–9.3)	13.0
Str2	Stromboli NW	4	2000– 2600	8 –3	60	166	101	2.4	9.7	3.5	100	800	215	Sinuous to arcuate	Mostly downslope asymmetrical	3.0 (–5)	26.0
Str3	Stromboli N	6	2300– 2600	4 –2	97	253	162	3	9.6	4.5	120	800	364	Sinuous to arcuate	Mostly downslope asymmetrical	0.4 (–2.3)	18.0

Pan1	Panarea NE	100	1800–2500	8 –3	305	800	528	8.8	47	25	1300	2000	1630	Sinuous to arcuate	Mostly downslope asymmetrical	2.6 (–7.3)	17.0
Vul1	Vulcano SW	20	800–1200	6 –2	122	280	152	4	11.8	7.5	600	2200	1300	Sinuous to arcuate	Mostly downslope asymmetrical	0.6 (–2)	32.0
Lipa 1	Lipari W	8	870–1260	5 –4	166	414	299	14	21	16	300	700	500	Arcuate	Mostly downslope asymmetrical	4.0 (–1.8)	32.0
Str4	Stromboli island (Piscità Channel)	3	30–174	10 –7	20	86	38	1.2	5	2.6	20	122	44	Arcuate–crescentic	Downslope asymmetrical	9.0 (–5)	28.0
Sal1	Salina Island (N)	3.3	285–677	11 –2.3	44	215	108	1.3	6.2	3.2	60	310	190	Arcuate–crescentic	Downslope asymmetrical	4.2 (–11.5)	29.5
Sal2	Salina Island (E)	3.8	45–430	14 –2	12	153	42	0.2	5.4	1.6	11	184	45	Arcuate–crescentic	Downslope asymmetrical	9.0	30.0
Vul2	Vulcano Island (NW)	0.8	200–450	9 –3	30	106	40	1.2	3.8	2	24	160	70	Arcuate–crescentic	Downslope asymmetrical	2.3 (–7)	26.0
Vul3	Vulcano Island (LFC)	0.2	70–200	9 –7	21	62	35	0.7	2.8	1.3	25	80	50	Arcuate	Downslope asymmetrical	6.0	15.0
	Vulcano Island (NE, Baia di Levante fan)	2	500–800	7 –5	36	92	66	1	4	2	70	250	140	Sinuous	Downslope asymmetrical	5.0 (–1)	18.0
Vn1	Tanna Island (Siwi Channel)	1.2	30–>208	9 –2	4	180	20	0.3	6	1.85	10	460	240	Crescentic to irregular	Asymmetrical upslope	4.0	28.0
Vn2	Tanna Island	0.5	50–>208	9 –1	5	75	18	0.2	8.5	1.3	50	250	150	Crescentic	Asymmetrical	4.0	29.0

	Coalesent Channel													to irregular	upslope		
Vn3	Tanna Island Single Channel	0.1	75–167	15 – 1	13	42	25	1.2	3.8	2.3	50	273	68	Crescentic to irregular	Asymmetrical upslope	4.0	24.0
Vn4	Tanna Island Channel Field (incl. Broad Channel)	0.7	155–>208	15 –1	12	60	30.5	0.5	5.8	1.95	699	1045	755	Crescentic to irregular	Asymmetrical upslope	5.0	43.0
MA1	E Desertas, downslope of landslide	1900	2900–4300	3.8 –0.5	746	3014	1575	5	31	16	26	46	*	Sinuous	Change between upslope asymmetrical and symmetrical	2.0 (–3.3)	11.6
	E Desertas, downslope of scours			4.7 –0.2	1016	4352	2154	8	47	20				Sinuous	Change between upslope asymmetrical and symmetrical	0.7 (9.3)	7.9
MA2	S Porto Santo	150	3250–4000	2.3 –0.4	1369	2322	1548	7	37	23	4	8	*	Sinuous	Change between upslope asymmetrical and symmetrical	*	0.0

MA3	N Porto Santo, inside channels	1500	2400–3600	3 –0.9	228	983	587	2	16	7	35	70	*	Crescentic downslope	Change between upslope and downslope asymmetrical and symmetrical	1.8 (–4.7)	21.0
	N Porto Santo, top of interfluves		2500–3500	5 –0.6	706	3463	1248	4	35	15				Crescentic uslope	Change between upslope and downslope asymmetrical and symmetrical	4.4	12.7
MA4	N of Madeira	3600	2000–4000	3.2 –1.2	388	3421	1095	4	61	16	46	52	*	Sinuous	Change between upslope asymmetrical and symmetrical	1.7 (–9.1)	10.6
MA5	NE of Madeira	600	2900–3600	2.8 –0.6	437	2456	1145	1	24	12	5	30	*	Sinuous	Change between upslope asymmetrical and symmetrical	1.3 (–3.6)	6.7
SEL1	SE of Selvagem Pequena	180	2300–3400	5.3 –1.8	345	1542	857	2	42	13	26	46	*	Sinuous	Change between upslope asymmetrical	4.0 (–3.7)	12.5

														and symmetrical		
	SE of Selvagem Grande			4.7 –0.2	188	1071	641	1	17	7				Sinuous	Change between upslope asymmetrical and symmetrical	1.4 (–4.8)	7.6
SEL2	NW of Selvagem Grande	20	3000–3400	3.3 –2.6	339	772	627	2	16	6	2	3	*	Crescentic upslope/downslope	Change between upslope asymmetrical and symmetrical	0.5 (–1.5)	8.9
SEL3	NE of Selvagem Pequena	25	2800–3400	3.5 –1.8	439	1026	559	4	35	12	1.5	3	*	Crescentic downslope	Change between upslope asymmetrical and symmetrical	2.1 (–4.6)	9.9
SEL4	SW of Selvagem Pequena	50	3300–3600	1.2 – 0.2	198	784	449	1	10	3	3	4	*	Sinuous	Change between upslope and downslope asymmetrical and symmetrical	0.8 (–2.6)	3.4

Table 2 Summary of grain-size, local boundary conditions and preconditioning and triggering mechanism for the recognized bedforms.

ID*	Location	Grain-size	Morphological setting	Volcanic regime	Meteo-Marine regime	Preconditioning and trigger mechanisms
MC1	Macauley	Unknown (only onshore grain sizes available)	Unconfined open slope	Hawaiian – Plinian	Prone to tropical cyclones and storms	Eruption-fed density currents
MC2	Macauley	Unknown (only onshore grain sizes available)	Unconfined open slope	Hawaiian – Plinian	Prone to tropical cyclones and storms	Eruption-fed density currents
MC3	Macauley	Unknown (only onshore grain sizes available)	Confined within sector collapse/Unconfined downslope	Hawaiian – Plinian	Prone to tropical cyclones and storms	Probable slope failure
MC4	Macauley	Unknown (only onshore grain sizes available)	Confined within sector collapse/Unconfined downslope	Hawaiian – Plinian	Prone to tropical cyclones and storms	Probable slope failure
MC5	Macauley	Unknown (only onshore grain sizes available)	Confined within sector collapse	Hawaiian – Plinian	Prone to tropical cyclones and storms	Probable slope failure
MC6	Macauley	Unknown (only onshore grain sizes available)	Confined within sector collapse/Unconfined downslope	Hawaiian – Plinian	Prone to tropical cyclones and storms	Probable slope failure
Zd1	Zavodovski	Unknown	Confined within gully/Unconfined downslope	Strombolian/Vulcanian	Exposed to southern ocean storms and swell	Initial slope failure followed by eruption-fed density currents
Zd2	Zavodovski	Unknown	Confined within gully	Strombolian/Vulcanian	Exposed to southern ocean storms and swell	Probable slope failure
Zd3	Zavodovski	Unknown	Confined within gully/Unconfined downslope	Strombolian/Vulcanian	Exposed to southern ocean storms and swell	Initial slope failure followed by eruption-fed density currents
DC2	Dakataua	Unknown	Unconfined open slope	Plinian/Sub-	Prone to tropical cyclones and storms	Sediment density flow/deformational creep

	Caldera			plinian/Phreatoplinian	with extreme rainfall	
DC1	Dakataua Caldera	Unknown	Unconfined open slope	Plinian – Vulcanian (Pheatoplinian – Phreatovulcanian)	Prone to tropical cyclones and storms with extreme rainfall	Sediment density flow/deformational creep
KB	Kimbe Bay	Unknown	Unconfined open slope	Plinian/Phreatoplinian	Prone to tropical cyclones and storms with extreme rainfall	Sediment density flow/deformational creep
Str1	Stromboli SE	Backscatter zonation on TOBI mosaic, strong echo on S.B.P.; coarse-sand and gravel at surface	Furrows just below a marked decrease of slope gradients	Strombolian activity	Microtidal regime, wind from SE waves up to 6 m	Sedimentary gravity flows from subaerial-submarine depression left by sector collapses
Str2	Stromboli NW	Backscatter zonation on TOBI mosaic, strong echo on S.B.P.; coarse-sand and gravel at surface	Turbidite troughs above a volcaniclastic fan due to the emplacement of debris avalanche deposits; associated with decrease of slope gradients	Strombolian activity	Microtidal regime, wind from N–NW waves up to 6 m	Sedimentary gravity flows from subaerial-submarine depression left by sector collapses
Str3	Stromboli N	Backscatter zonation on TOBI mosaic, strong echo on S.B.P.; coarse-sand and gravel at surface	Channel at the base of the saddle between Stromboli and Strombolicchio	Strombolian activity	Microtidal regime, wind from SE waves up to 6 m	Sedimentary gravity flows from subaerial–submarine depression left by sector collapses and from retrogressive slope failures at the edge of insular shelf
Pan1	Panarea NE	Not available	Unconfined at the base of the Panarea N flank	Lava domes and subordinate explosive activity	Microtidal regime, wind from SE waves up to 6 m	Channels draining the submarine flanks from retrogressive slope failures at the edge of insular shelf
Vul1	Vulcano SW	Coarse-grained volcaniclastic layer in a 1.6 m long core	Unconfined on a fan-shaped feature	Vulcanian-type activity	Microtidal regime, wind from SE waves up to 6 m	Sedimentary gravity flows from two wide shallow water scars, partially affecting also the subaerial flank of the edifice
Lipa 1	Lipari W	Not available	Confined within a straight channelized	Hydromagmatic and Strombolian activities	Microtidal regime, wind from SE waves up to 6 m	Retrogressive erosion at the edge of the insular shelf

			feature			
Str4	Stromboli island (Piscità Channel)	Sandy	Flat-bottomed channel in the saddle between Stromboli and Strombolicchio	Strombolian	Microtidal regime, wind from SE waves up to 6 m	Flat-bottomed channels in a saddle, fed by longshore drift during eruptive crisis
Sal1	Salina Island (N)	Sandy	Flat-bottomed channel below the shelf edge	Subplinian (last eruption 15.6 ka)	Microtidal regime, wind from SE waves up to 6 m	Retrogressive erosion at the edge of the insular shelf
Sal2	Salina Island (E)	Sandy	Channels-fan/large channel	Strombolian to subplinian (last eruption 13 ka)	Microtidal regime, wind from SE waves up to 6 m	Channels morphologically linked to steep creeks onland draining pyroclastic rocks
Vul2	Vulcano Island (NW)	Sandy	Flat-bottomed channel	Vulcanian-type activity	Microtidal regime, wind from SE waves up to 6 m	Retrogressive erosion at the saddle between Vulcano and Lipari and Vulcanello isthmus
Vul3	Vulcano Island (LFC)	Sandy	Gullies within La Fossa Caldera	Vulcanian-type activity	Microtidal regime, wind from SE waves up to 6 m	Sedimentary density flows flow from the dismantling of La Fossa Caldera infilling
	Vulcano Island (NE, Baia di Levante fan)	Sandy	Fan-shaped feature below La Fossa Caldera	Vulcanian-type activity	Microtidal regime, wind from SE waves up to 6 m	Sedimentary density flows flow from the dismantling of La Fossa Caldera infilling
Vn1	Siwi Channel Bedform field	Fine to medium sand (based on ROV surface sampling)	Within and on outer edge of caldera collapse, which has defined location of channels	Strombolian	Prone to significant tropical cyclones and storms with extreme rainfall, which can trigger elevated river discharges (>1000 m^3/s). This particular bedform field may be linked to a volcanic lake outburst flood in AD 2000	Sedimentary density flows
Vn2	Coalesent Channel	Fine to medium sand (based on ROV surface sampling)	Within and on outer edge of caldera collapse, which has defined location of	Strombolian	Prone to significant tropical cyclones and storms with extreme rainfall, which can trigger elevated river	Sedimentary density flows

			channels		discharges (>1000 m^3/s)	
Vn3	Single Channel	Fine to medium sand (inferred from ROV sampling in nearby areas)	Within and on outer edge of caldera collapse, which has defined location of channels	Strombolian	Prone to significant tropical cyclones and storms with extreme rainfall, which can trigger elevated river discharges (>1000 m^3/s)	Sedimentary density flows
Vn4	Bedform Channel Field (incl Broad Channel)	Fine to medium sand (inferred from ROV sampling in nearby areas)	Immediately seaward of caldera collapse	Strombolian	Prone to significant tropical cyclones and storms with extreme rainfall, which can trigger elevated river discharges (>1000 m^3/s)	Sedimentary density flows
MA1	E Desertas, downslope of landslide	No information	Landslide scar upslope	Mostly Hawaian activity	Microtidal regime, wind from SE waves up to 1.2 m	Probable slope failure or sedimentary density flows over irregular debris deposits
	E Desertas, downslope of scours	No information	Channels upslope, located where gradients decrease to less than 5˚	Mostly Hawaian activity	Microtidal regime, wind from SE waves up to 1.2 m	Sedimentary density flows flows from passage from confined to unconfined setting; abrupt slope break
MA2	S Porto Santo	No information	Landslide scar upslope	Mostly Hawaian activity	Microtidal regime, wind from SE waves up to 1.2 m	Probable slope failure or sedimentary density flows over irregular debris deposits
MA3	N Porto Santo, inside channels	Lee side shows high backscatter	Inside channels	Mostly Hawaian activity	Microtidal regime, wind from NW waves up to 5.2 m	Sedimentary density flows from erosion of channel
	N Porto Santo, top of interfluves	Lee side shows high backscatter	Landslide scar upslope	Mostly Hawaian activity	Microtidal regime, wind from NW waves up to 5.2 m	Probable slope failure or sedimentary density flows over irregular debris deposits
MA4	N of Madeira	No information	Landslide scar upslope	Mostly Hawaian activity	Microtidal regime, wind from NW waves up to 5.2 m	Probable slope failure or sedimentary density flows over irregular debris deposits (profiles MAD1 and MAD2) or sedimentary density flows from passage from confined to

						unconfined setting; abrupt slope break (profile MAD2)
MA5	NE of Madeira	Lee side shows high backscatter	Landslide scar upslope	Mostly Hawaian activity	Microtidal regime, wind from NW waves up to 5.2 m	Probable slope failure or sedimentary density flows over irregular debris deposits
Sel1	SE of Selvagem Pequena	No information	Downslope of submarine ridge linking the two islands	Mostly Hawaian activity	Microtidal regime, wind from SE waves less than 1 m	Sedimentary density flows from volcanic activity
	SE of Selvagem Grande	No information	Channels upslope, located where gradients decrease to less than 5º	Mostly Hawaian activity	Microtidal regime, wind from SE waves less than 1 m	Sedimentary density flows from erosion of channel and passage from confined to unconfined setting; abrupt slope break
Sel2	NW of Selvagem Grande	Lee side shows high backscatter	Channels upslope, located where gradients decrease to less than 5º	Mostly Hawaian activity	Microtidal regime, wind from NE waves up to 4.3 m	Sedimentary density flows from erosion of channel and passage from confined to unconfined setting; abrupt slope break
Sel3	NE of Selvagem Pequena	Lee side shows high backscatter	Channels upslope, located where gradients decrease to less than 5º	Mostly Hawaian activity	Microtidal regime, wind from NE waves up to 4.3 m	Sedimentary density flows from erosion of channel and passage from confined to unconfined setting; abrupt slope break
Sel4	SW of Selvagem Pequena	No information	Scour scar upslope	Mostly Hawaian activity	Microtidal regime, wind from NE waves up to 4.3 m	Scour upslope, sediment density flows from erosion of scour

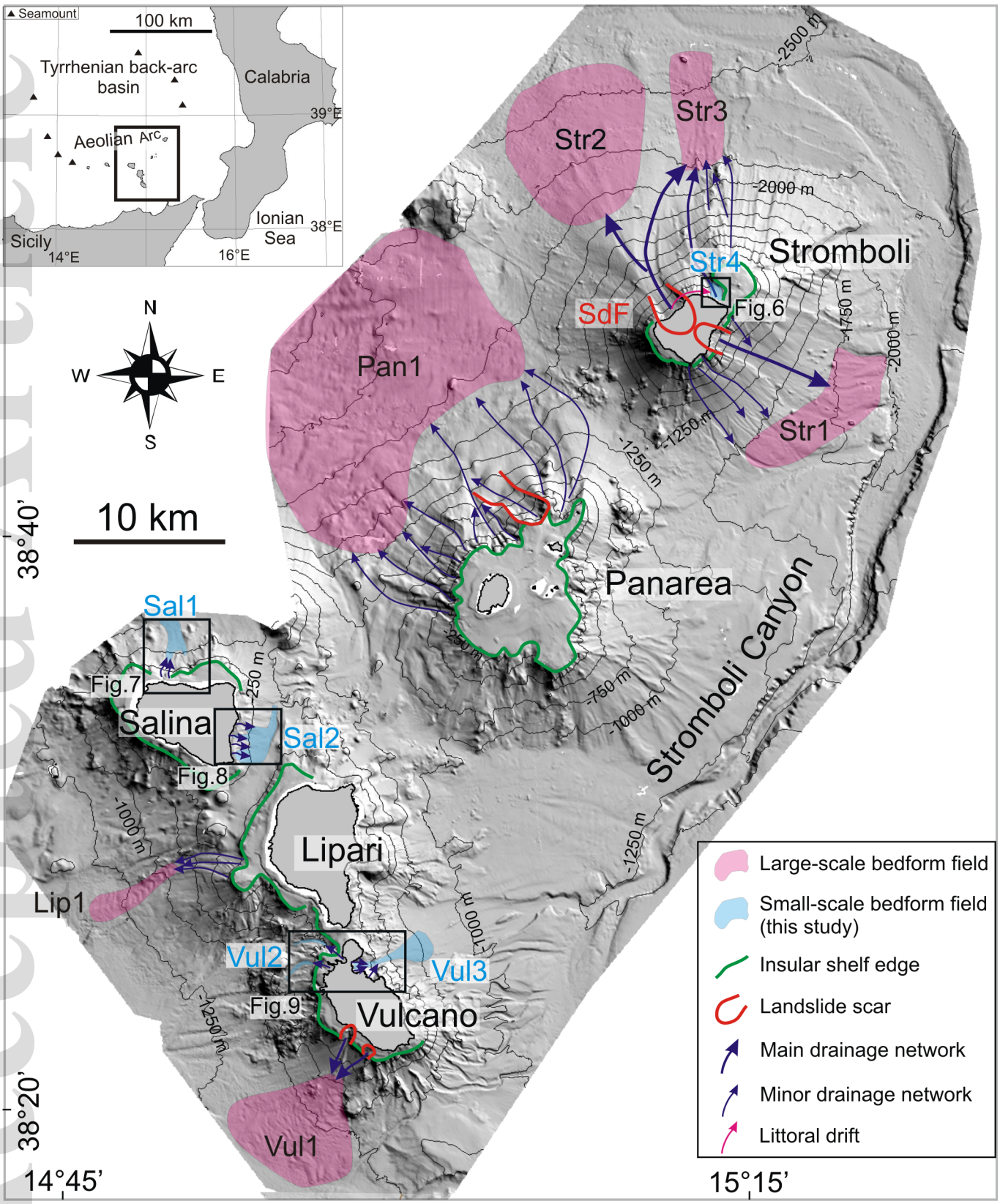

sed_12725_f1.tif

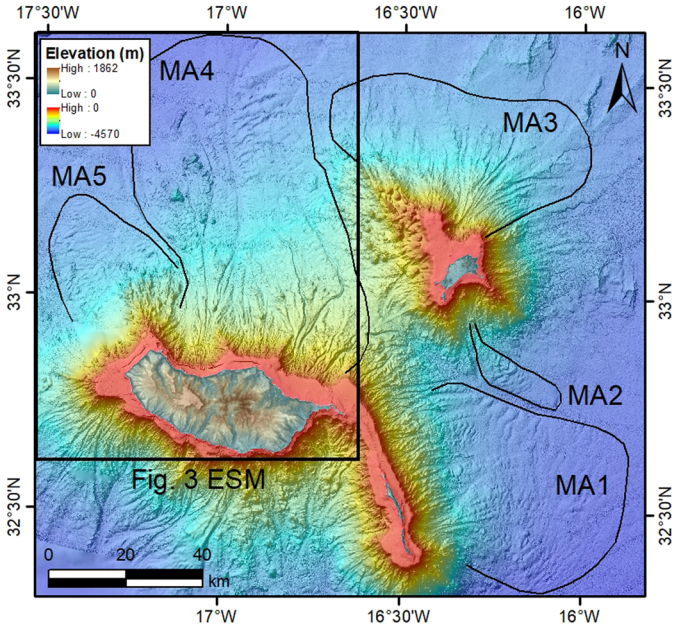

sed_12725_f2.tif

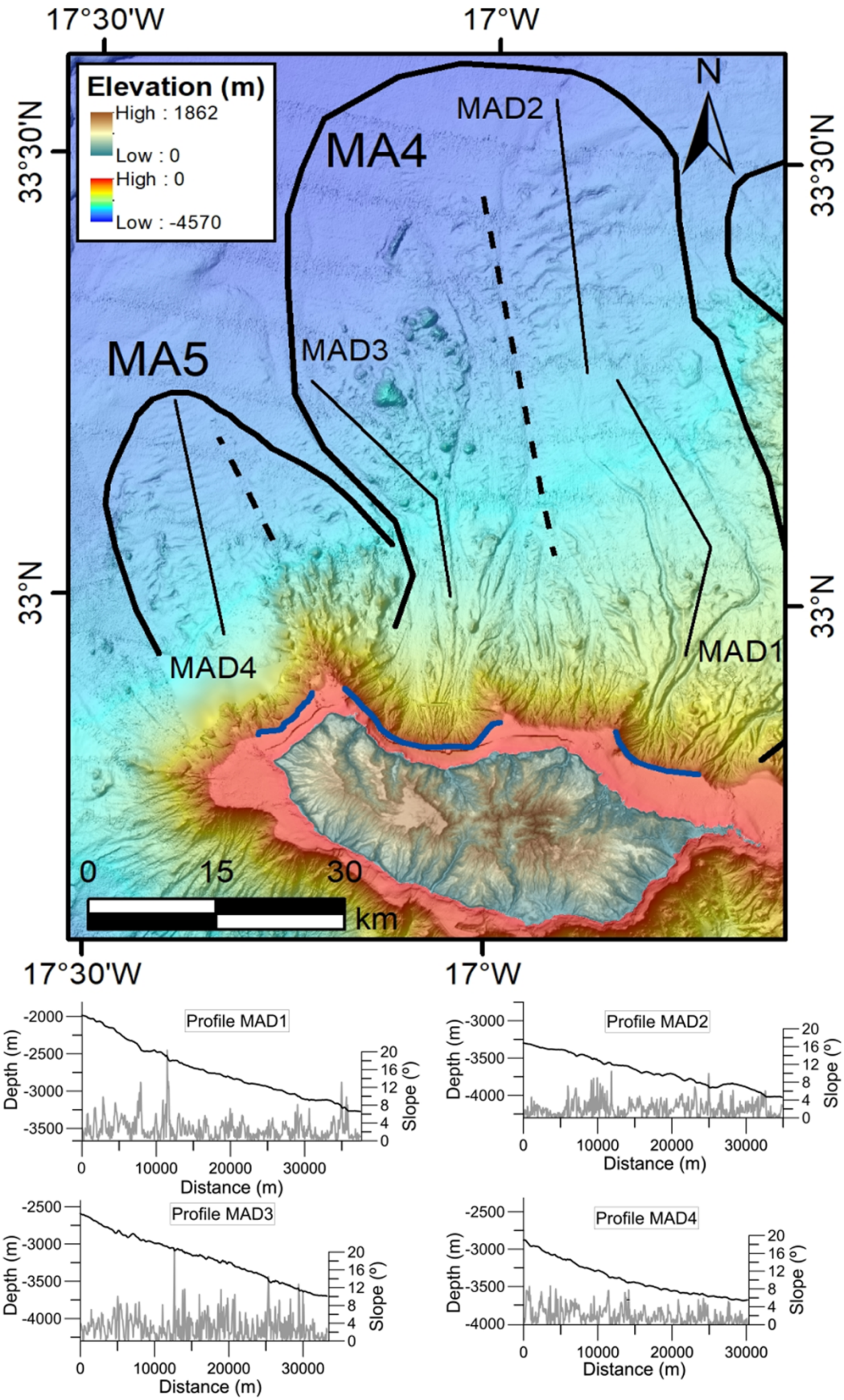

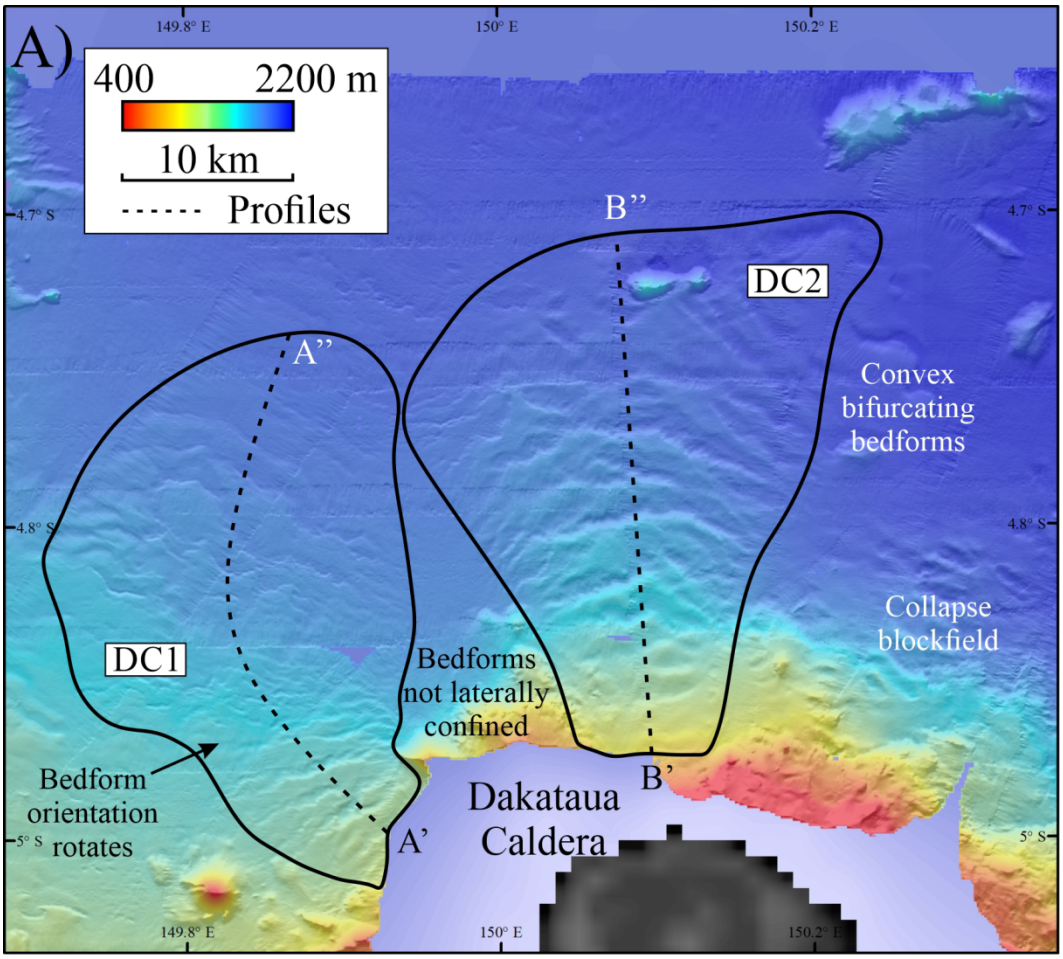

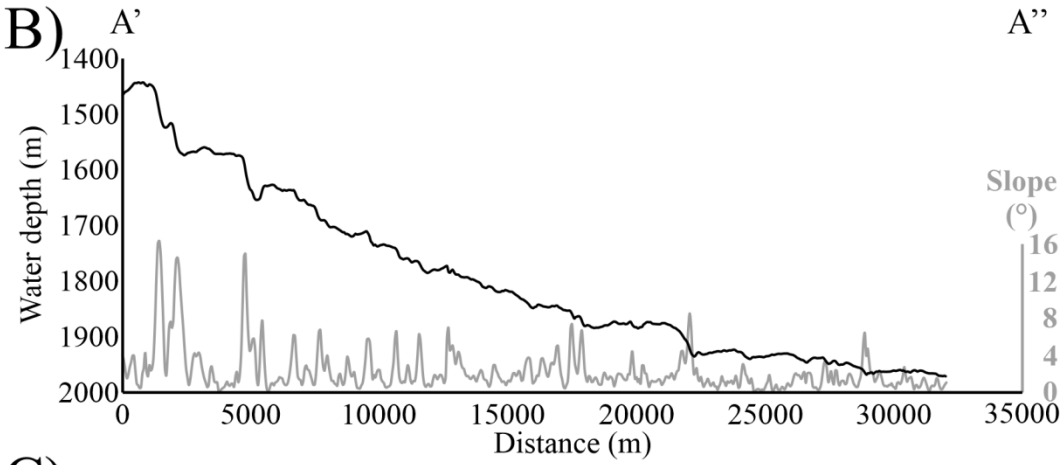

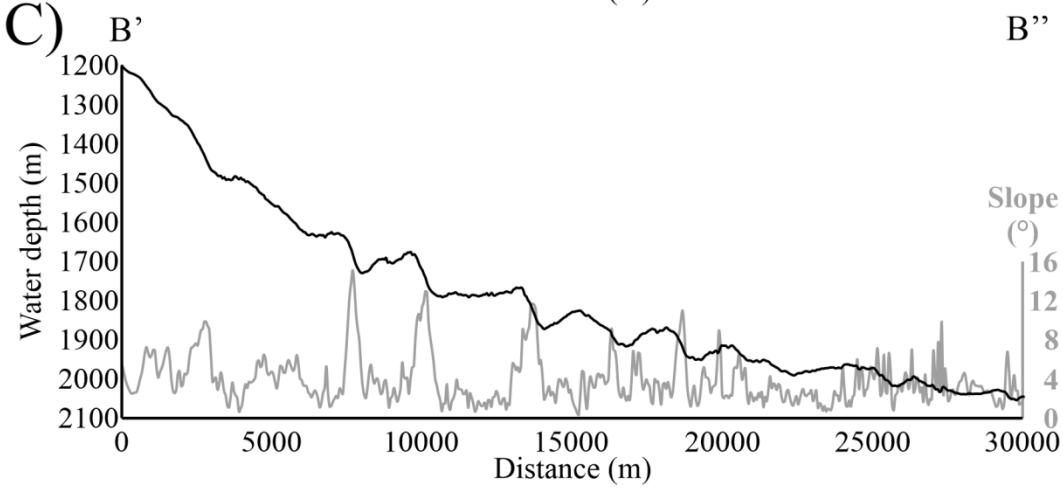

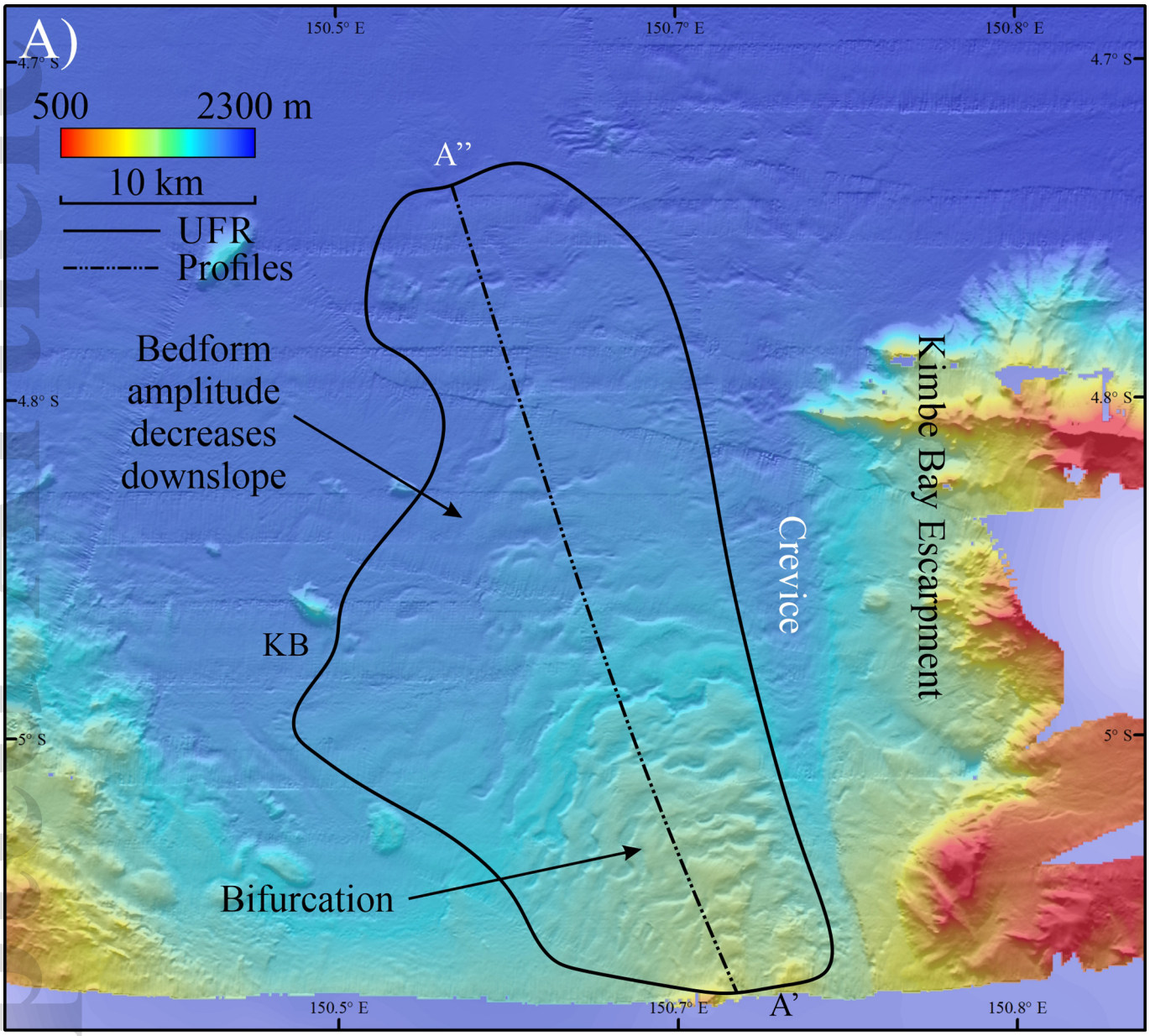

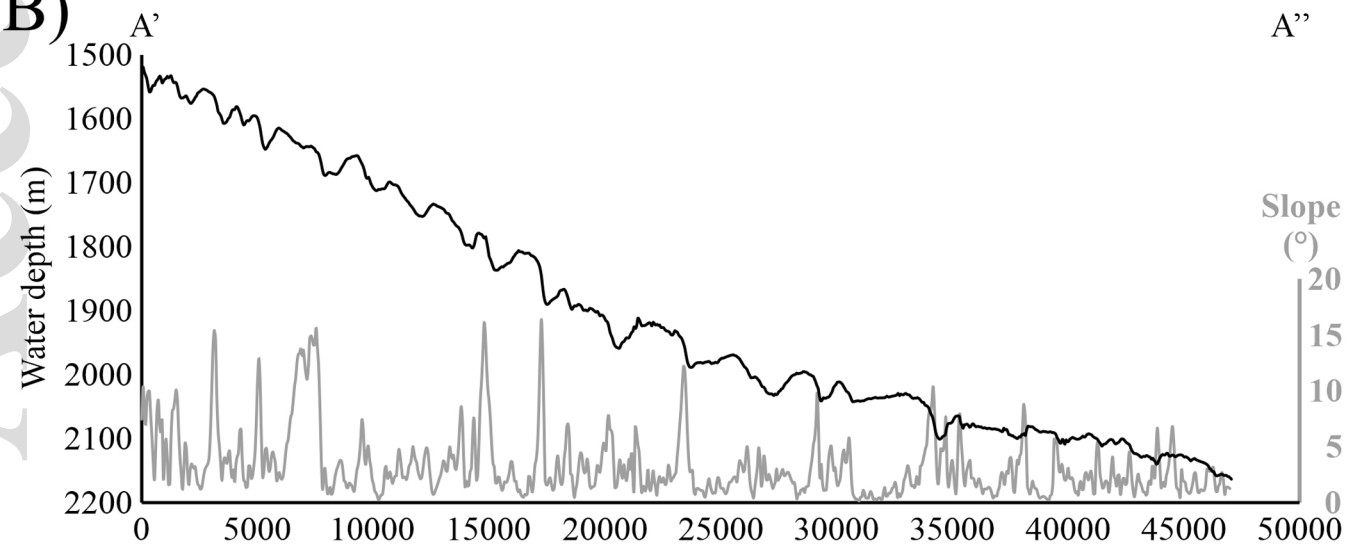

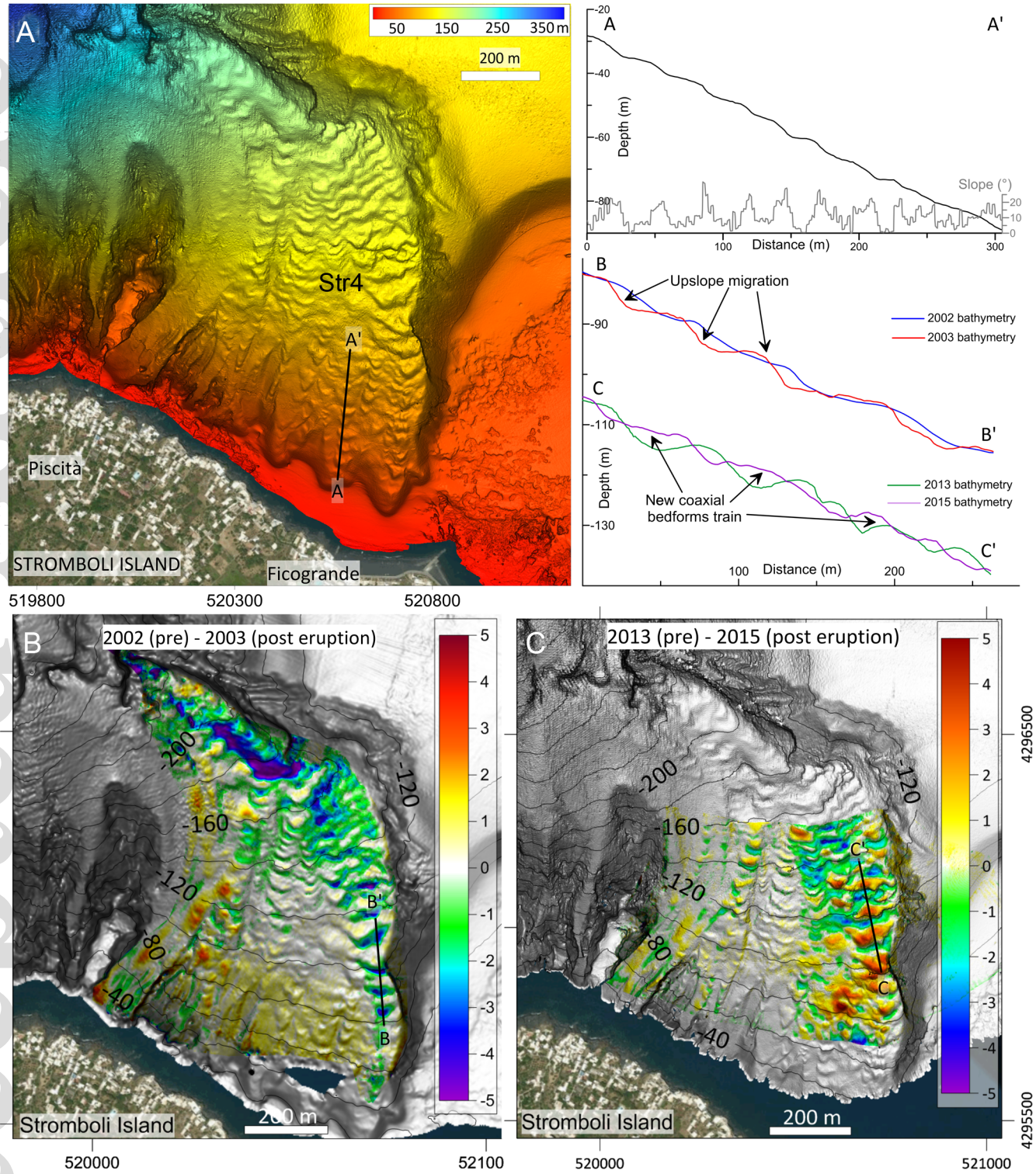

sed_12725_f6.tif

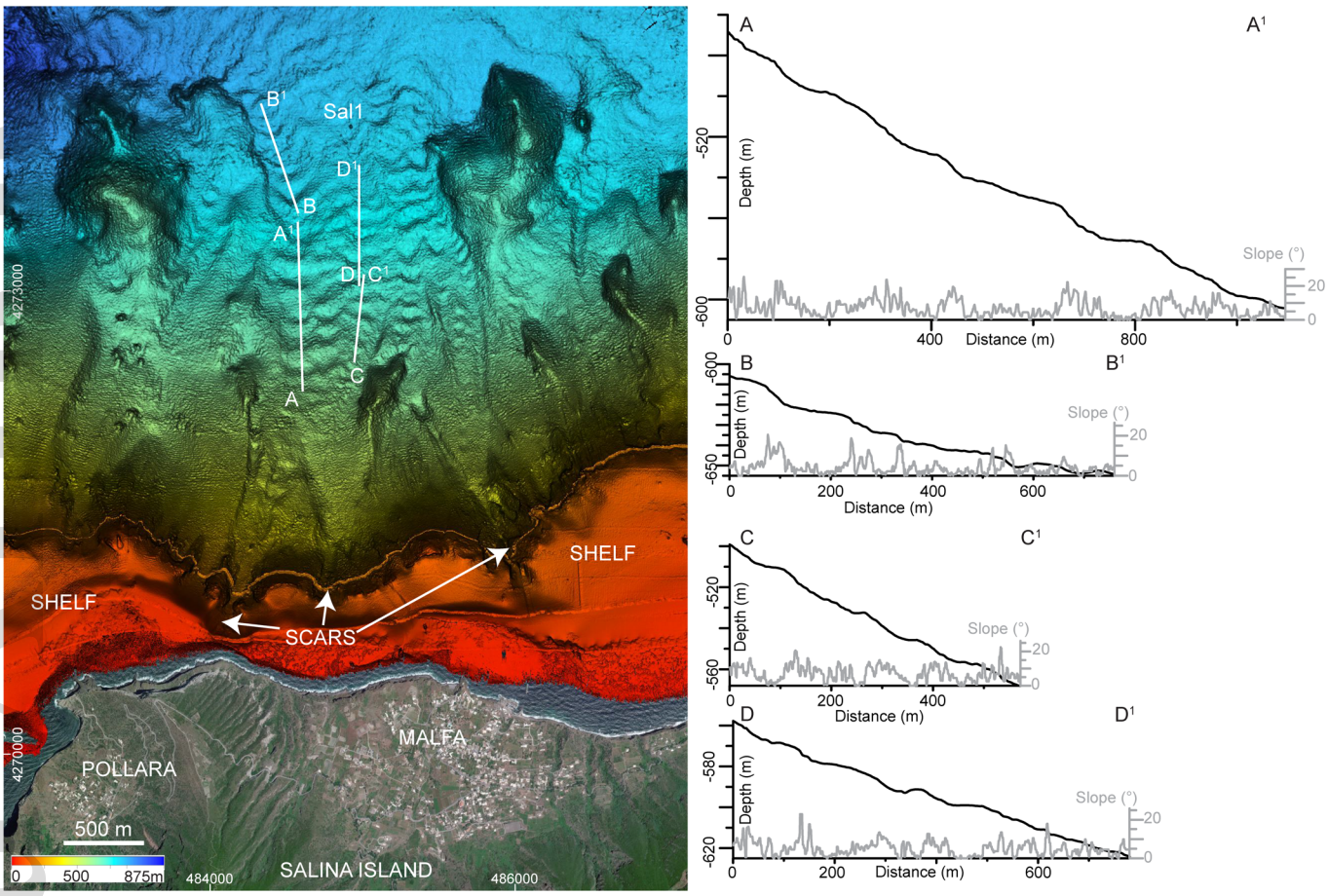

sed_12725_f7.tif

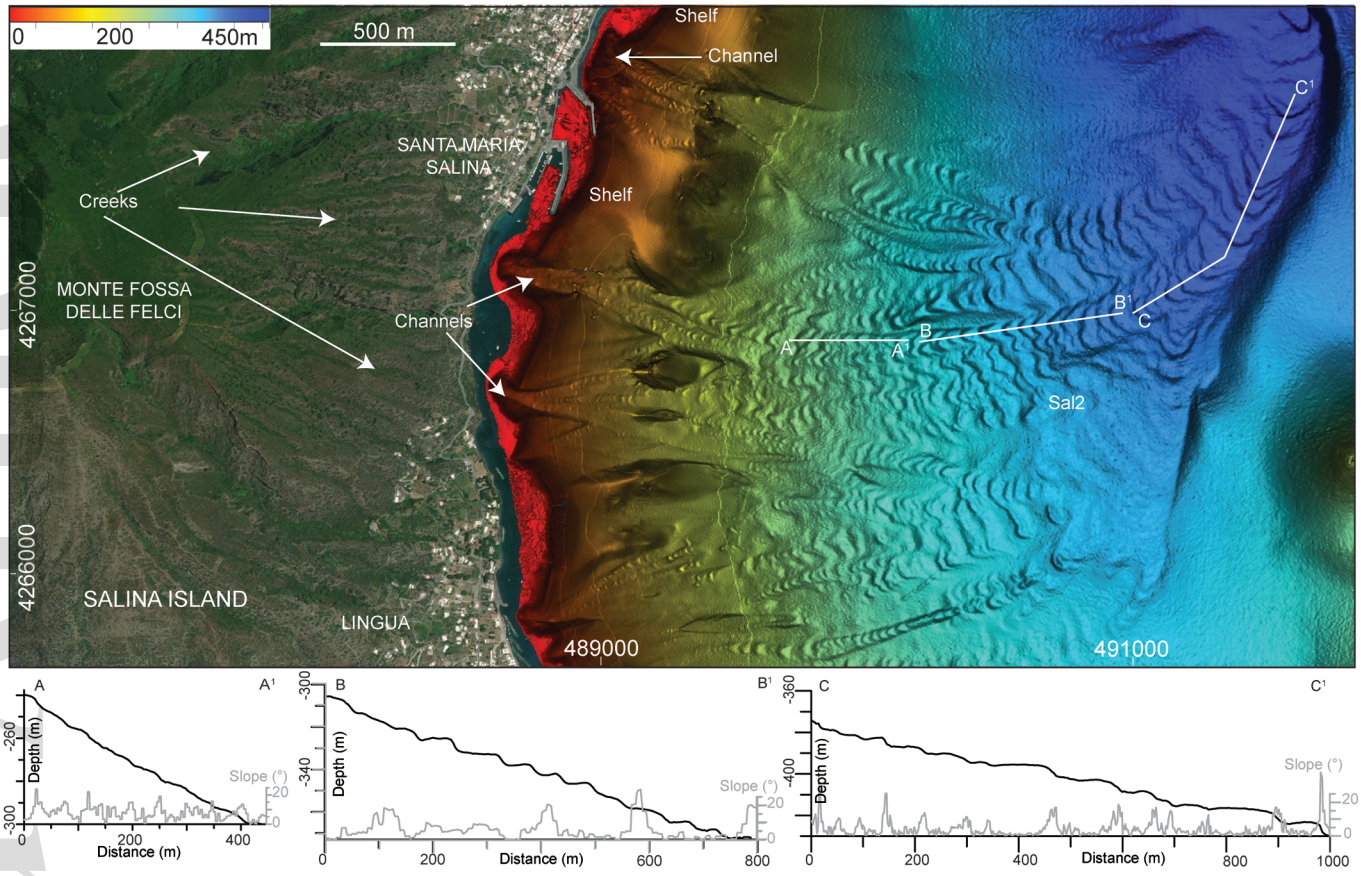

sed_12725_f8.tif

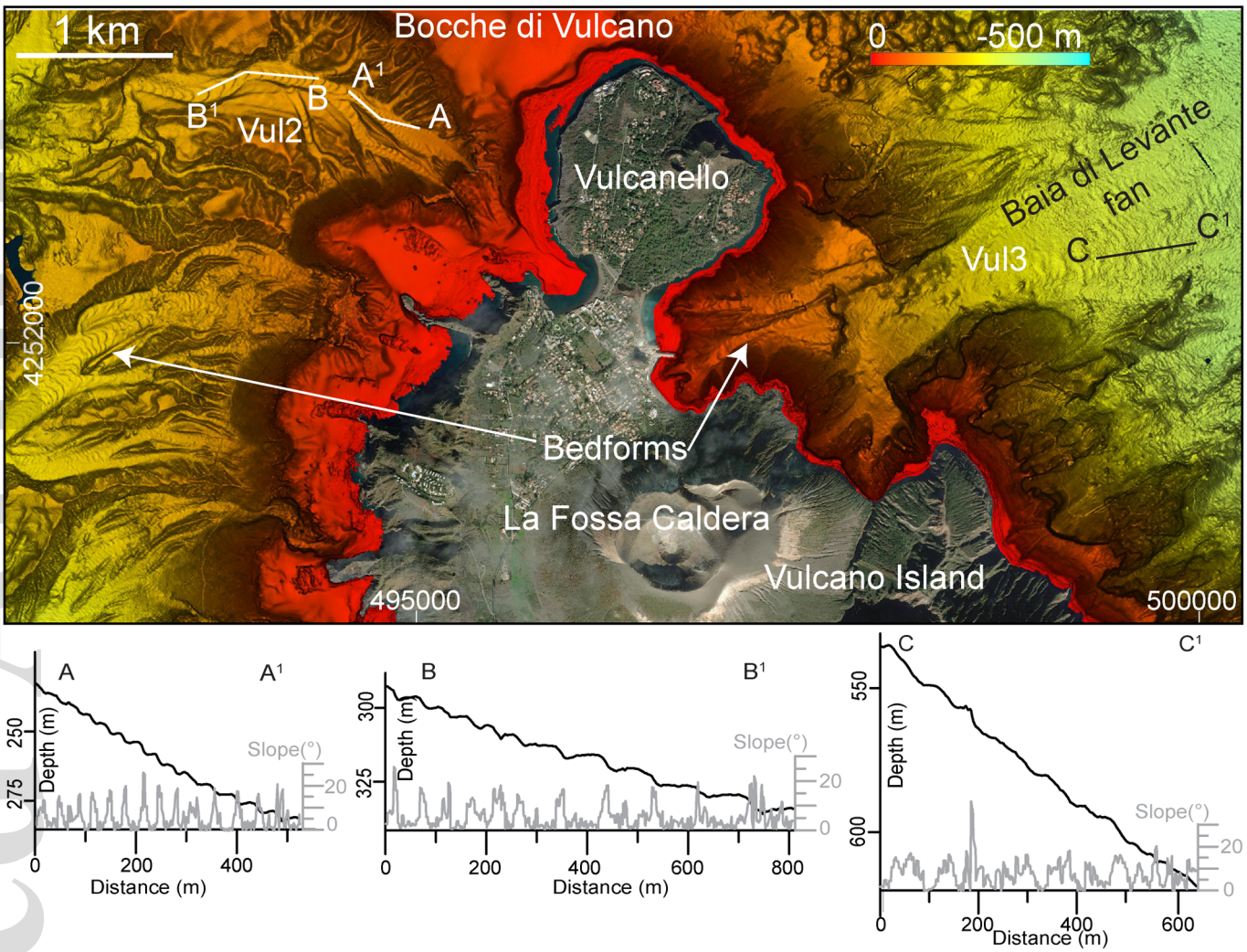

sed_12725_f9.tif

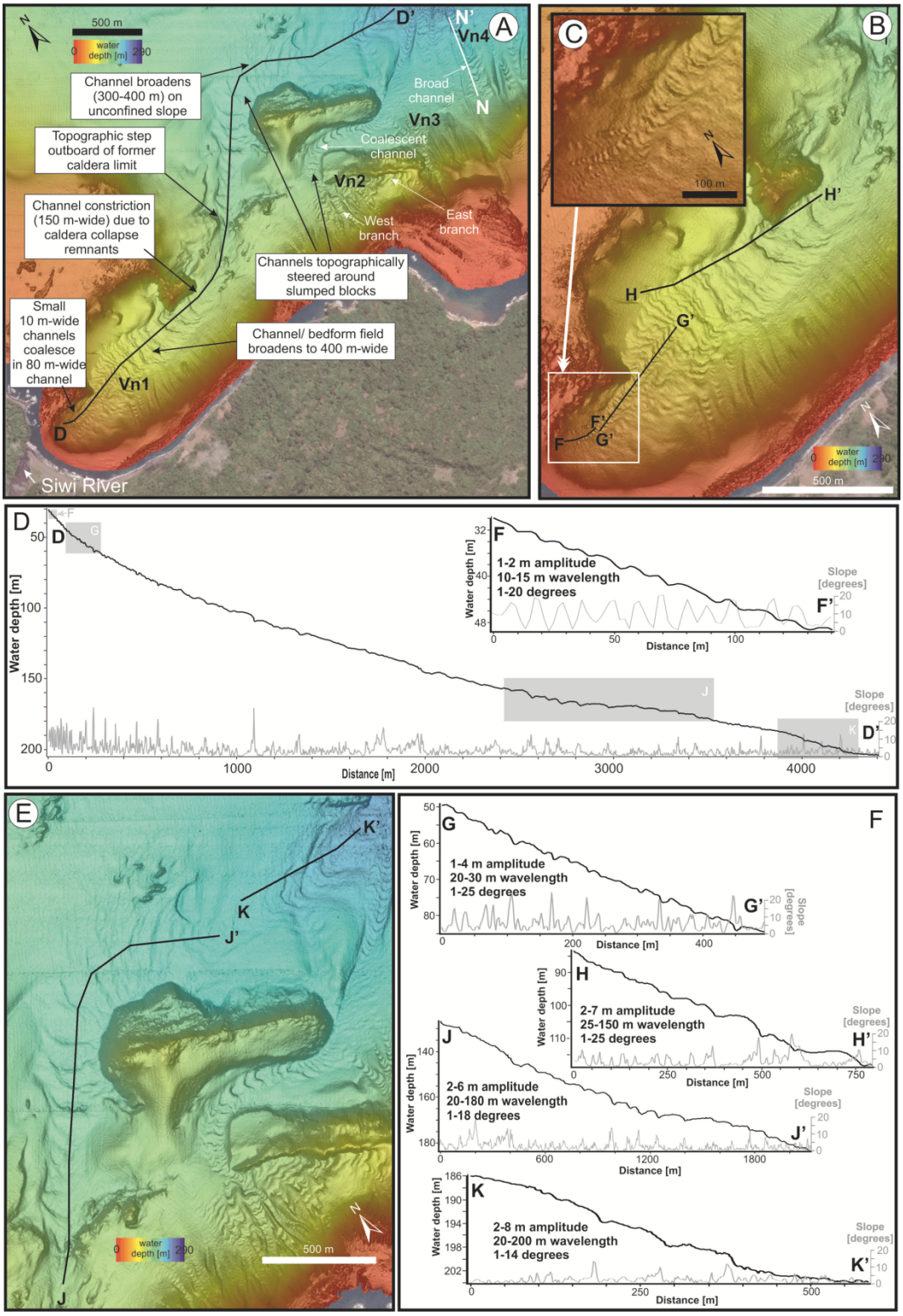

sed_12725_f10.tif

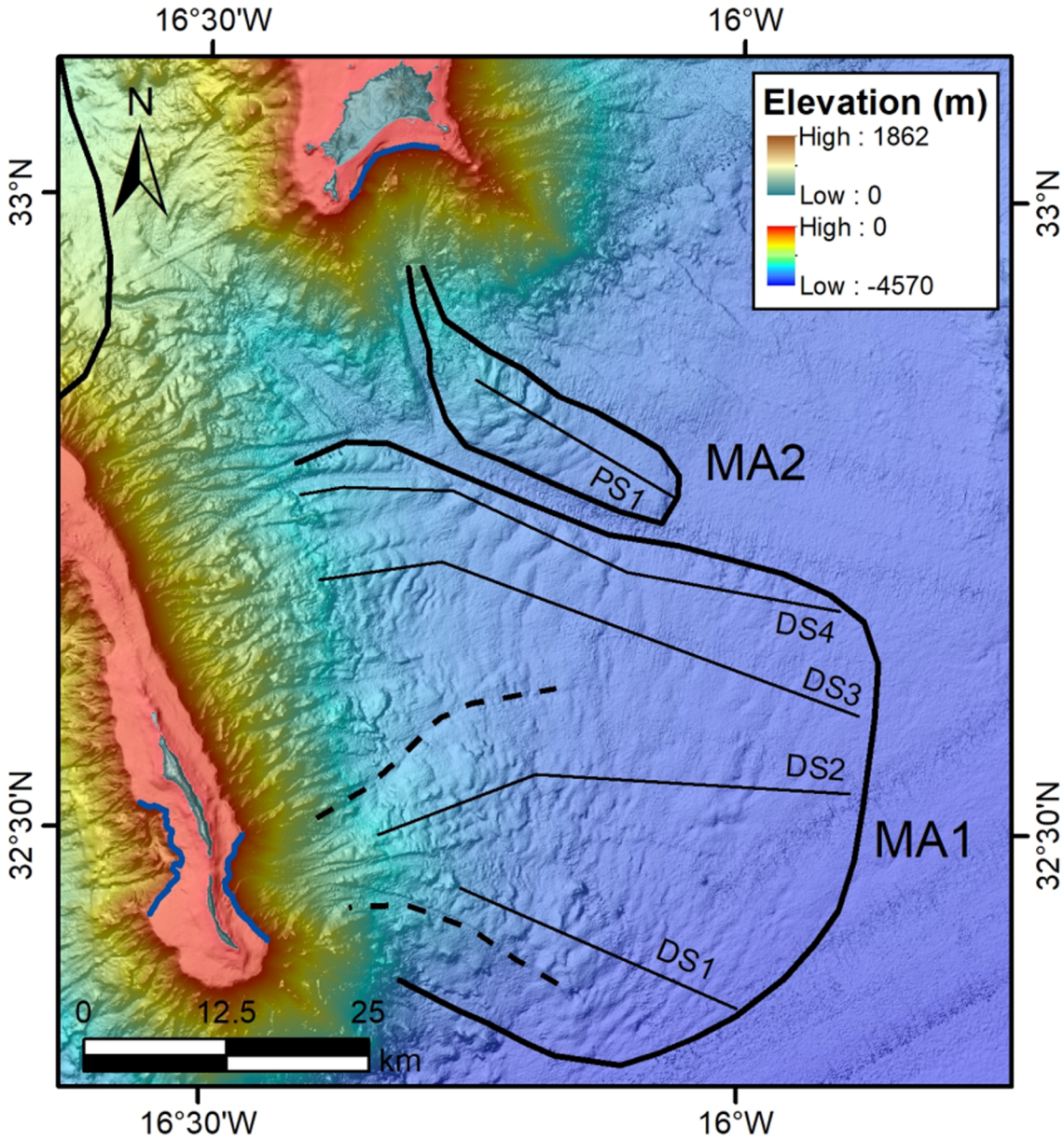

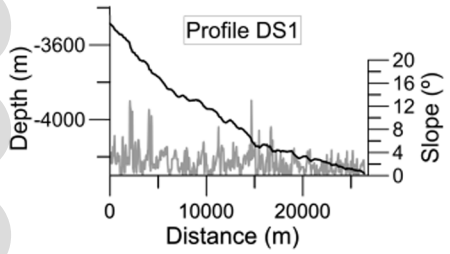

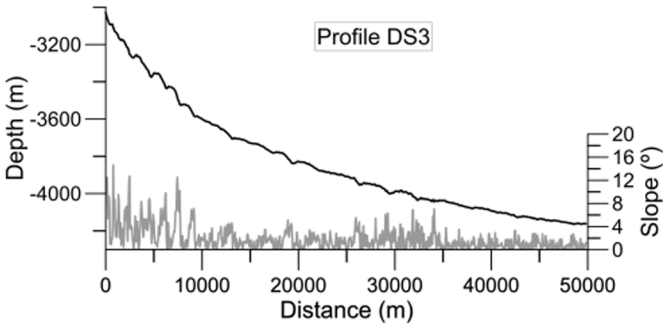

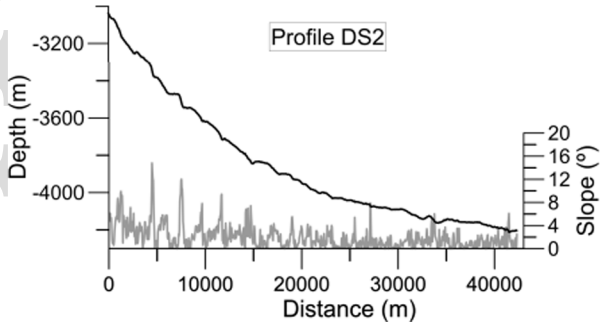

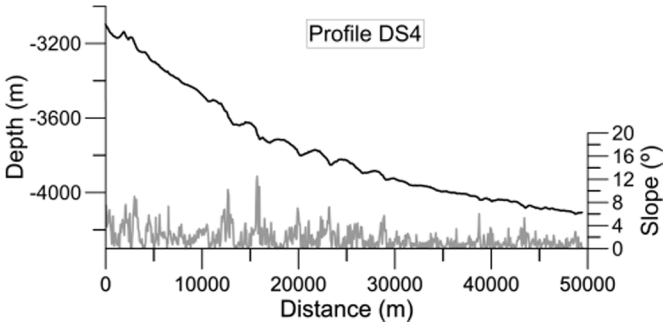

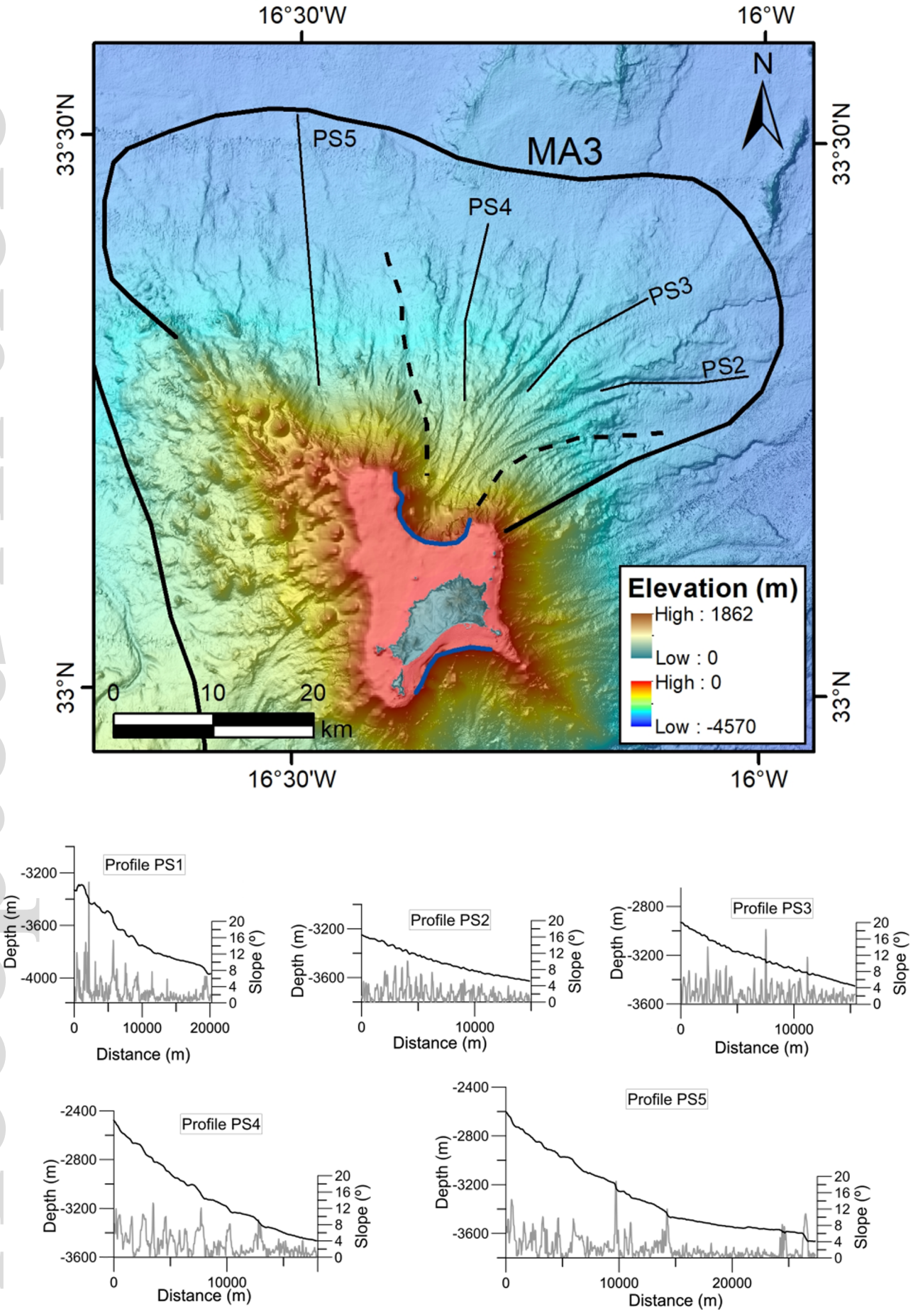

sed_12725_f12.tif

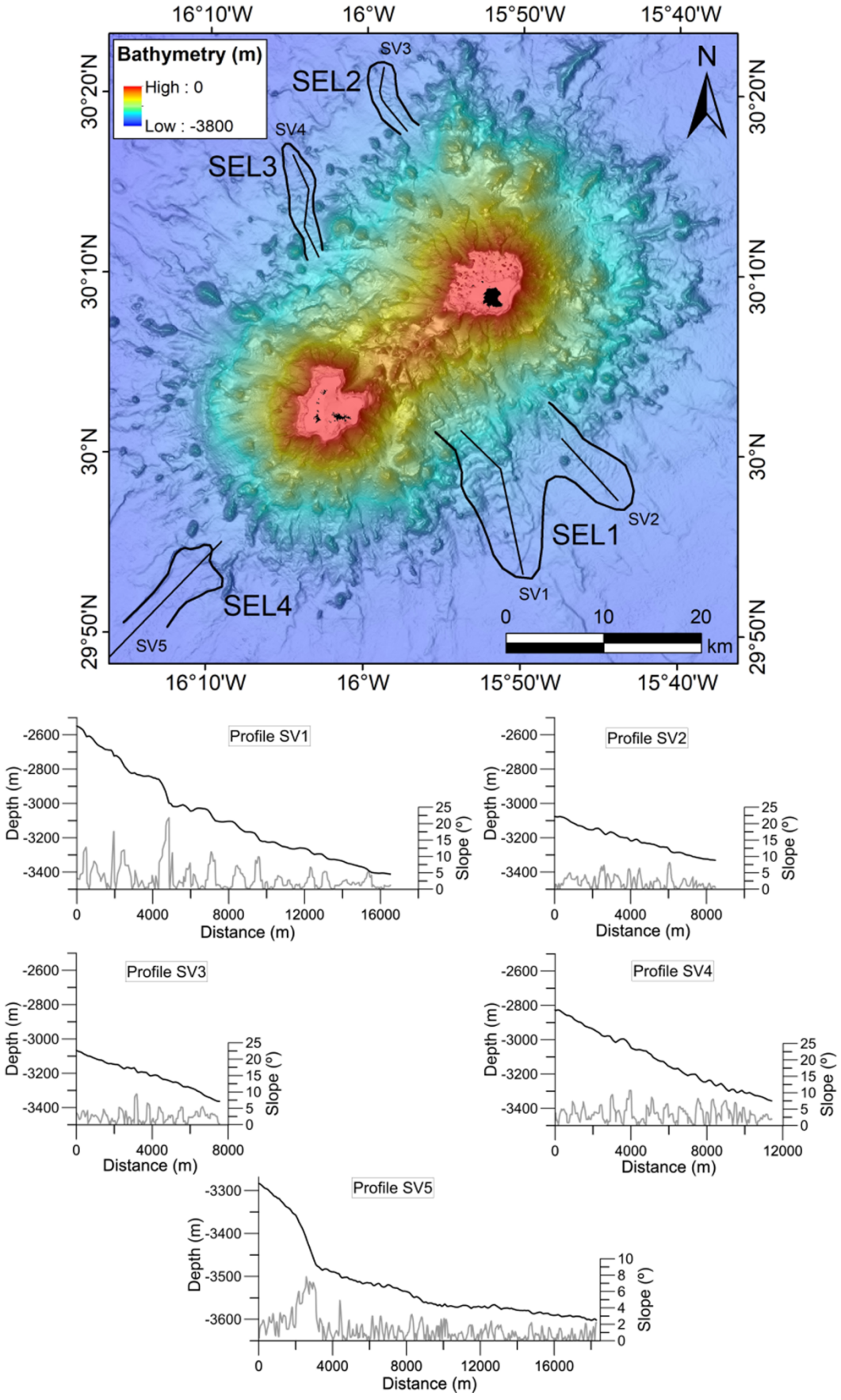

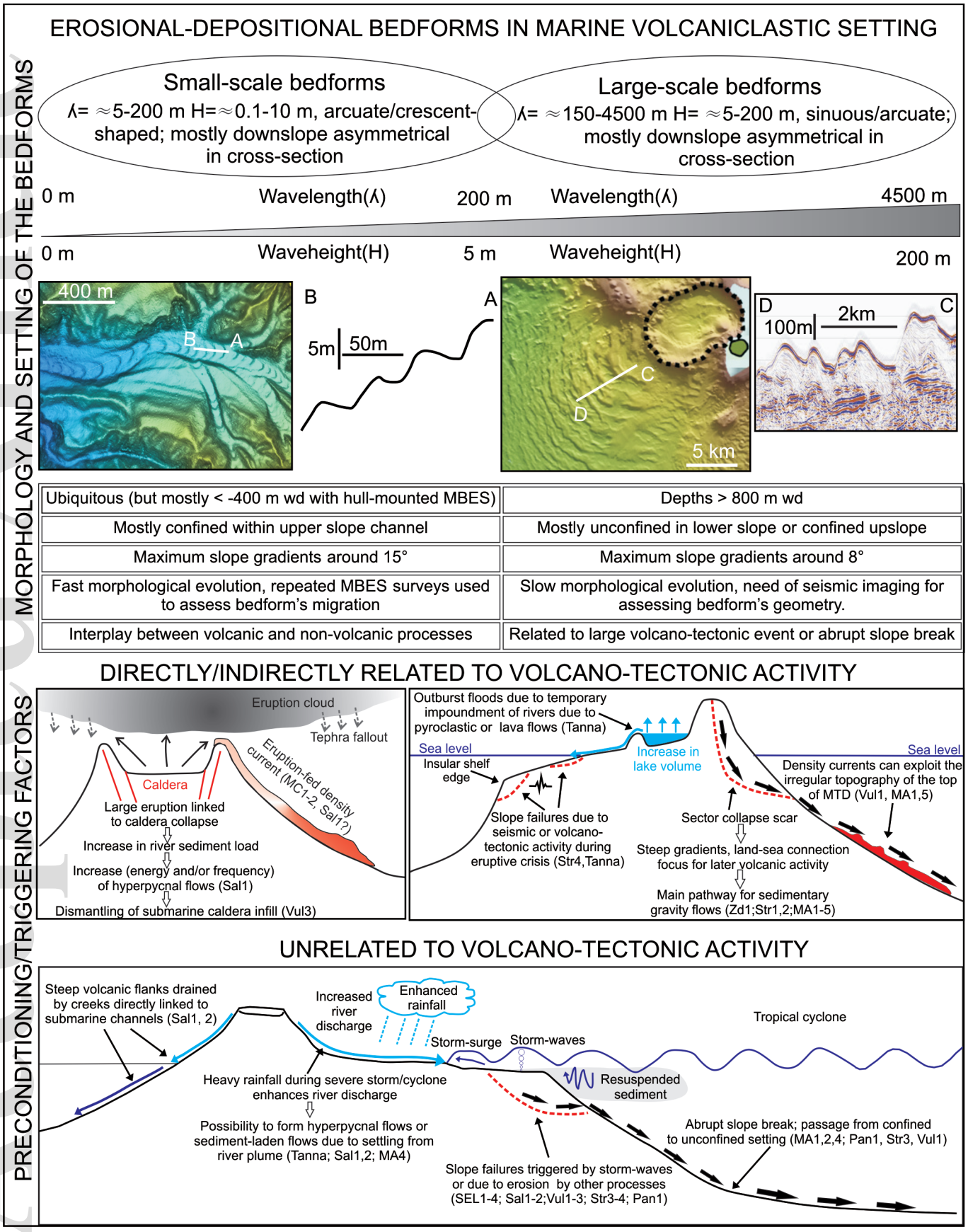

sed_12725_f14.tif

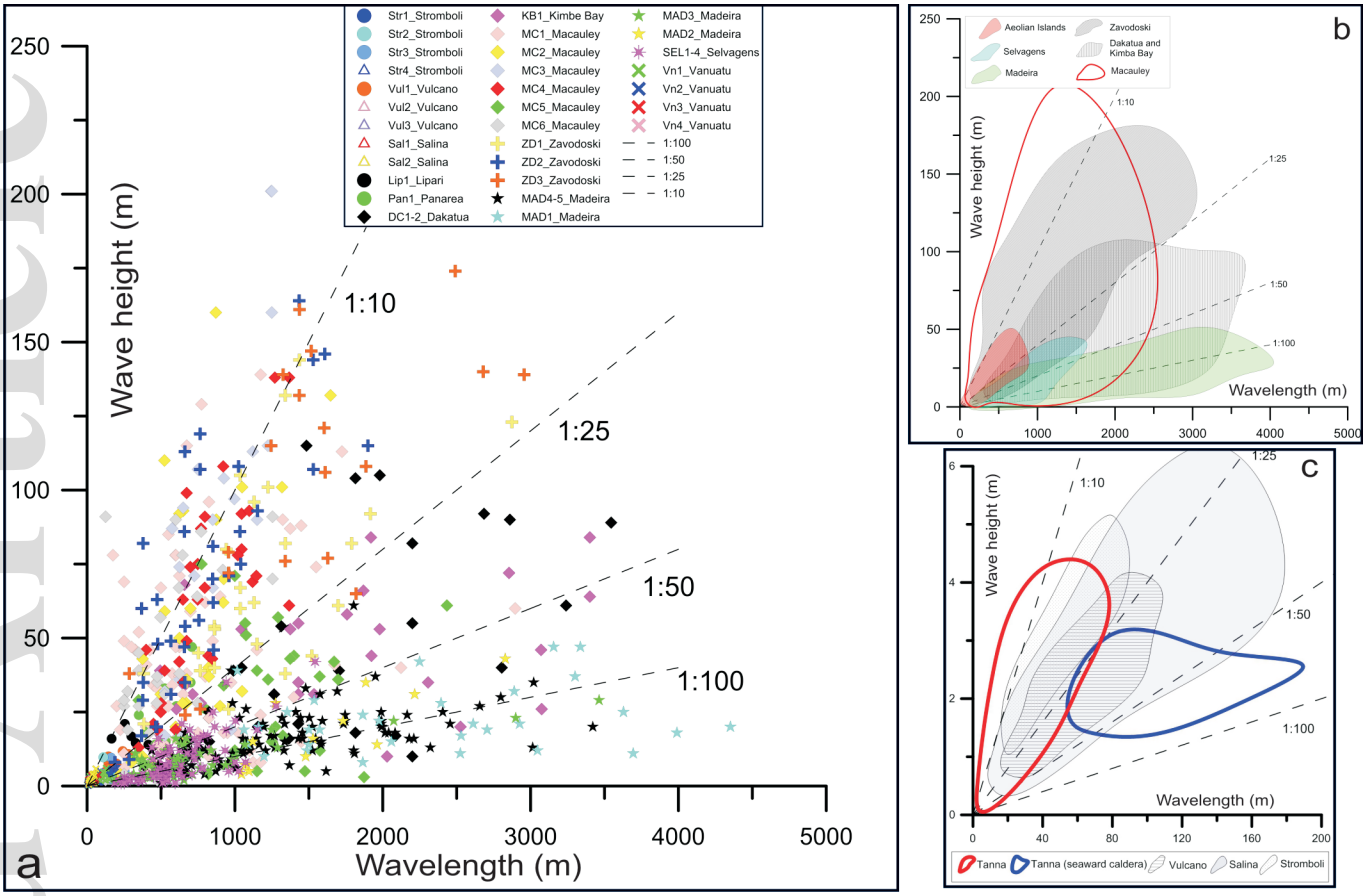

sed_12725_f15.tif